IN FLIGHT CALIBRATION OF THE PSF

FOR THE MOS1 AND MOS2 CAMERAS.

EPIC-MCT-TN-011   Simona Ghizzardi

October 8, 2001

S. Ghizzardi - Milano Calibration Team - Istituto di Fisica Cosmica "G. Occhialini"- CNR - Milano

e-mail: simona@ifctr.mi.cnr.it

Contents

1 Introduction

In this document, I present the results concerning the calibration of the on-axis and off-axis PSF using in orbit data. Data concern both MOS cameras and include observations performed in different operating modes (Full Frame, Double Node, Large Window, Small Window) with different filters.

The document is organized according to the following main topics:

- In Sec. 2, I will describe the data set used for the calibration;

- In Sec. 3, I will review the procedures adopted for the construction and the fit of the PSF profiles. A completely analytical modelization of the PSF will be introduced in §3.2.1.

- In Sec. 4 the results of the calibrations will be presented and discussed.

2 The data set.

The data set includes observations taken both in the commissioning phase and in the calibration and performance verification phase. They concern revolutions from 22 to 96. The off-axis angles of the observed sources range from 0.02 to 11.90 arcmin.

I have also analyzed the star field OMC2/3 in revolution 237. Within this stellar field, I selected all the sources with more than 20 photons in the peak. Accordingly, 14 sources have been selected for the MOS 1 and 16 for the MOS 2. The sources with an unreliable determination of all the fit parameters for all the energies have been rejected: for the MOS 1, 3 sources have been rejected, for the MOS 2 none. For the resulting set of sources of this field, the off-axis angles range from 2.03 to 10.42 arcmin for the MOS 1 and from 0.34 to 10.44 arcmin for the MOS 2. So, this stellar field has the advantage of covering a wide range of aff-axis angles; however the selected sources are not intense and the wings are not well sampled. Furthermore, often the small distance between the stars reduces the radial range useful for the fit and makes the determination of the background uncertain. Consequently, this field provides best fit parameters only for the energies from 1 to 4-5 keV where the statistics is high enough to provide reliable fits.

Depending on the observation (presence of pile-up effect, bad statistics on the wings, etc), it can occur that a measure can provide only informations on the core or on the wings. A large fraction of the observed sources have a count rate high enough to induce pile-up effects. In these cases, we don't have any information about the core of the PSF, but the

wings can be studied. If a corresponding observation (same source and pointing position but different filter and/or operating mode, i.e. different pile-up levels) exists, we can study simultaneously the core and the wings. Often (especially for off-axis angles $\gtrsim 5'$, where only Full Frame mode is possible) only piled-up data are available. As a result, we will have a very precise estimate of the wings of the PSF, but a poorer evaluation of the core.

As the PSF depends on the energy, **we divided the whole spectral range [0-12 keV] in different intervals: [200-400], [400-800], [800-1200], [1200-2400], [2400-5000], [5000-8000], [8000-12000] eV, corresponding to mean energies 0.3, 0.6, 1, 1.8, 3.7, 6.5, 10 keV.**

As will be discussed in §4.4, in the whole data set, no observation at large ($\gtrsim 4'$) off-axis angles has enough counts to allow an inspection at high (6.5-10 keV) energies. **Correspondingly, in these cases, no calibration data exist and no conclusion can be drawn.**

In Table 3, we list all the observations included in the analysis, with their RUNID, the off-axis angle (in arcmin), the operating mode (FF=Full Frame, DN=Double Node, LW=Large Window, SW=Small Window, TI=Timing). The observations listed within the same box in the table have been merged together. **In fact, whenever it was possible, we joined different observations in order to enhance the statistics.** The techniques used for the merging will be described in details in §3.1.1.

Some observations have not been included in the sample for different reasons:

- HR1099 in revolution 36 and 3C273 in revolution 94 with off-axis angles $\sim 6'$: the measures are visibly piled-up within the central $15''$; the choice of the range of fit (see §3.2.4) is delicate and it can affect the best fit results. On the other hand, the high statistics of the measure produces a very small error on the best fit parameters. Such fit parameters must be rejected because unreliable and having very small errors can drive the final fit.

- Capella in rev. 53 with off-axis angles $\sim 5'$ and $\sim 10'$: these measures have a very strong pile-up, producing a large central hole (about $40''$ wide). Neither the core nor the wings can be investigated.

- GX13+1 has a central hole ($15''$) due to a strong pile-up. The pile-up probably affects the profile also in the region just outside the central hole, providing distortions in the profile. The distortions are less important for the low ($\lesssim 1$ keV) and for the high energies (~ 10 keV). Only points which are not affected from the pile-up can be retained. This occurs only in the very outer part of the profile (at a radius $\sim 1.5'$)

3

where the statistics and the dynamic range are too small even for the evaluation of the wings.

In the field of GX13+1, there is a small secondary source which has been included in the sample and which is here referred to as GX13+1b. Analogously, Capella2 refers to a small source visible in some pointings on Capella. The two sources in the pointings of the revolution 22 (05:37:04; -69:13:00.0) have been referred to as LMC1 and LMC2.

3   The analysis procedure.

Our main purpose is to construct the radially averaged profile of each source of the sample and for each selected energy range and successively to fit it with a suitable function. In this section, I will review the procedures for building and fitting (respectively in paragraphs 3.1 and 3.2) the radial profiles of the sources, starting from the source events lists. All the analysis procedures are developed in IDL language.

All the observations have been filtered in order to have "cleaned" event lists, where bright/dark pixels/columns have been removed and the events associated to the soft protons have been discarded. For all the runs, **only patterns ≤ 12** have been considered.

3.1   Building the radial profiles.

In this paragraph, we will describe in detail the algorithm developed to build the radial profile of each source. The procedure can be divided into three main steps: i) merging of similar observations; ii) determination of the centroid, and iii) construction of the radially averaged profile of the PSF. Each of these points is discussed in detail in the following paragraphs.

3.1.1   Stacking similar observations.

In order to enhance the statistics whenever possible we merged together similar observations. Specifically, I joined observations having the following requirements:

1. same source target;

2. same pointing direction;

3. same operating mode (FF, DN, LW, SW);

4. same filter position.

Obviously we merged together observations separately for the two MOS cameras.

Usually, the merging operation simply consists in stacking the different event lists. Of course, the pointings of the observations to be merged together must be exactly the same.

After this merging operation, we divided the data into groups. Merged data sets concerning the same target and with the same pointing position but with different operating mode and/or filter position, i.e. with different pile-up levels, are included in the same group. We identified 86 (39 for MOS 1 and 47 for MOS 2) groups, each having the same source target and the same pointing position (i.e. the same off-axis angle).

3.1.2 Getting the centroid.

In order to build the radial profiles, we must define the centroid for each image. The centroid finding is quite a delicate procedure. In fact, we cannot simply identify the centroid with the peak (the pixel with the greatest number of photons). It can lead to biased results for faint sources where there are only few photons in the peak and the statistical fluctuations are important. Besides, the method surely cannot be applied to piled-up observations where the peak and the inner region are damped. In particular, when the piled-up is strong a central hole appears. In this case, locating the centroid is obviously difficult.

However, also when the pile-up is absent or is weak, the centroiding must be accurate as small shifts can induce distortions in the radial profile.

An additional difficulty is represented by the presence of the mask. In fact, the image can have dark (no counts) pixels because of the mask. We must implement an algorithm able to consider that the image "is not" zero in those pixels. Neglecting the mask can induce a shift in the final centroid coordinates. The problem of the mask becomes particularly important when the source is spread across two different CCDs.

The procedure I built goes through these steps:

1. It starts from an initial centroid $(xc0, yc0)$. It considers all the points within a radius *radcen* of 150 pixels from this centroid.

   If:

   - the source is near to the edge of the Field of View;
   - the source is not on-axis and the operating mode is Large Window;
   - the operating mode is Small Window;
   - the distance of the source with another source is less than 150 pixels;

and *radcen* cannot be so large, then *radcen* is taken as large as possible. In the first three cases it can be determined from the initial centroid and the detector mask. In the last case, it must be directly provided as a parameter. This occurs, for instance, for the sources of the stellar field OMC2/3.

2. In order get a stable result, a cut-off image is considered. This image is reduced from the original one, assigning a null value to all the pixels having less than $max/5$ counts, being max the highest number of counts stored in the image pixels. Correspondingly, only the brightest pixels are considered in the evaluation of the centroid. Besides providing a more robust result, this technique strongly reduces the computational time.

3. For the masked points, the algorithm assigns to the image an effective value obtained according the following procedure. Being (x, y) the masked pixel, the procedure considers the values I_2, I_3, I_4 of the image in the points $(x, 2 \cdot yc0 - y), (2 \cdot xc0 - x, 2 \cdot yc0 - y), (2 \cdot xc0 - x, y)$ which are symmetric to (x, y) with respect the centroid $(xc0, yc0)$. Then, the algorithm assigns the the pixel (x, y) a weighted average I_1:

$$I_1 = \frac{1}{4}I_2 + \frac{1}{2}I_3 + \frac{1}{4}I_4.$$

More complicated weighted averages are considered whenever one (or more) of these symmetric points has a null mask value.

4. The new centroid is calculated according to the formulae:

$$xc = \frac{\sum_{i,j} x_i N(x_i, y_j)}{\sum_{i,j} N(x_i, y_j)},$$

$$yc = \frac{\sum_{i,j} y_j N(x_i, y_j)}{\sum_{i,j} N(x_i, y_j)},$$

where $N(x_i, y_j)$ is the number of photons in the (x_i, y_j) pixel and the sum runs over the pixels inside *radcen*.

5. If the shift of the new resulting centroid (xc, yc) with respect to $(xc0, yc0)$ is too large (i.e., greater than *radcen*/10 or than 6 pixels if *radcen* is less than 100), the starting value $(xc0, yc0)$ is kept and the procedure is repeated with a slightly smaller *radcen*.

6. The $(xc0, yc0)$ is set to be (xc, yc) and the procedure is repeated recursively (for *radcen* progressively smaller) until the shift of the centroid is less than 1 pixel. In most of cases, this occurs after a few steps.

3.1.3   The radial profile algorithm.

For the event lists of each group, reduced event lists for the various energy ranges are selected. The radial profiles are calculated then separately for each energy range.

The procedure I developed for building the radial profiles, evaluates for each r the number of counts in the annulus between r and $r+dr$, divided the annulus area. Different binnings have been used for different radii. In the inner regions each bin is set to be equal to a pixel, for outer radii, bins are set to several pixels. In fact, for large r, the number of counts is not very high and a large binning enhances the statistics making the integration procedure faster without loss of accuracy. I divided the range (0-230) pixels in four regions with the following number of bins:

rmin: 0	rmax: 20	nbins: 20
rmin: 20	rmax: 40	nbins: 10
rmin: 40	rmax: 80	nbins: 10
rmin: 80	rmax: 230	nbins: 15

($rmin$ and $rmax$ are in pixels units).

In order to evaluate the number of pixels in each annulus, the procedure basically consists in storing, for each pixel of the image, the bin which the center of the pixel belongs to. It assigns the entire pixel to the corresponding bin updating the counts in the bin and its area summing the contribution of the pixel.

For inner pixels near the centroid of the PSF, assigning a (squared) pixel to a (radial) bin, according to the position of the pixel center, may be a rough approximation and this can introduce non negligible distortions in the final profile. In fact, near the centroid, where annuli curvatures are high, pixels can belong to different annuli in comparable fractions. Hence, the basic algorithm has been improved adding a recipe suited to split pixels which are not completely included within an annulus. More precisely, the procedure runs over all pixels within a region R enclosing the RMIN – RMAX region and slightly larger than this. For each pixel, it finds the bin b_i which the pixel center belongs to and it checks if the circle enclosing the pixel (same center, $r = \sqrt{2}/2$) is fully enclosed in the bin b_i. If so, then surely the same occurs for the whole pixel. In this case, the improved procedure "uses" the basic one, and updates counts in b_i and the area of the bin summing the contribution of the pixel. Otherwise, if part of the circle is not in the same bin, the pixel too could be partly inside another bin. In this case, the pixel is split into *nsubpixels* subpixels (set by the user); each subpixel is processed by itself and provides a contribution

to the counts equal to $image(pixel)/nsubpixels$ and to the area equal to $1/nsubpixels$. In the inner region a large number of subpixels is needed and it can be reduced at larger radii where the curvature is smaller and the effect is less important. Therefore, I set $nsubpixels$=100, 49, 16, 4 for the four binning ranges.

3.2 Fitting the radial profiles.

Once the radial profiles have been built, they have to be suitably fitted. Since the profiles are determined by radially averaging the counts in each bin, any angular distortion (which can be important for off-axis sources) is actually neglected. Therefore, the PSF model function f can be radially symmetric: $f = f(r)$. Starting from the ground calibration results, in §3.2.1, I build the analytical function which is suitable to describe the measured radial profile.

As previously pointed out, in order to have a more precise estimation of the PSF, whenever possible, we use simultaneously informations at different pile-up levels. Hence, I built an algorithm able to do a multi-fit, i.e. a simultaneous fit of several curves. The algorithm is described in detail in §3.2.2. The last two paragraphs of this section §3.2.3 and §3.2.4 deal with two delicate aspects of the fitting procedure: the background determination and the choice of the *good fitting range*.

3.2.1 Modeling the PSF

According to the ground calibration, the PSF could be fitted with a *King* + *Gauss* function:

$$PSF = A \left\{ \frac{1}{\left[1 + \left(\frac{r}{r_c} \right)^2 \right]^\alpha} + \frac{R}{\sqrt{(2\pi\sigma^2)}} \exp\left[-\left(\frac{r}{\sigma} \right)^2 \right] \right\}, \tag{1}$$

with 4 free parameters to be determined by fitting the data:

- r_c: the core radius of the (main) King component;

- α: the King slope;

- σ: the Gaussian amplitude;

- R: the relative normalization of the two components.

It is worth to note that both this function and its integral in $r\,dr$ are analytic. Correspondingly, both the PSF and the EEF are analytically characterized.

The Gauss component provides a correction to the King slope in the outer part of the wings which show a flattening at $r \sim \sigma$. The parameters depend on energy and off axis angle. The total normalization A depends on the total flux of the observation.

From ground calibration (on data concerning FM1) the values of the parameters where at 1.5 keV energy (on-axis pointing):

$$r_c = 6.668 \pm 0.640 \,(\text{arcsec});$$

$$\alpha = 1.748 \pm 0.021;$$

$$\sigma = 139.41 \pm 3.40 \,(\text{arcsec});$$

$$R = 2.69 \cdot 10^{-2} \pm 8.25 \cdot 10^{-3}.$$

(see S.G. EPIC-MCT-TN-001, http://www.ifctr.mi.cnr.it/∼simona/pub/ for details).

In considering the in-orbit model, we must account for two aspects: first of all, ground calibrations concerned the FM1 which is a spare camera. Thus, the parameters reported above cannot be compared to those from the in-flight data as they refer to different telescopes. Furthermore, for the in-orbit data, the presence of the X-ray background hides the Gauss component and the fit becomes insensitive to the Gaussian parameters. For this reason, we neglect the Gaussian component and the fitting curve is reduced to the King profile:

$$PSF = A \left\{ \frac{1}{\left[1 + \left(\frac{r}{r_c}\right)^2\right]^\alpha} + BKG \right\}. \tag{2}$$

A constant describing the background has been added. There are other possibilities to account for the background. The details are discussed in §3.2.3.

Actually, the fitting procedure uses the "complete" form of the function, *King + Gauss + bkg*, including the Gaussian component and only when the fit fails to converge or returns nonsense (e.g. negative or extremely large) values, the "reduced" *King + bkg* (eqn. (2)) is adopted. The details of the procedure are reported in the next paragraph.

3.2.2   Multi-fitting

As already pointed out the (merged) observations have been divided into 86 (39 concerning the MOS 1 and 47 the MOS 2) groups. In each group, data sets concerning the same target and with the same pointing position but with different pile-up levels are included.

I developed a fitting procedure capable of fitting simultaneously the different curves belonging to the same group, constraining the fit parameters r_c and α (and eventually σ and R) to be the same for all the profiles. Of course, the total normalization and the background constant are different for the different curves. For a set of n curves the fit parameters are therefore $r_c, \alpha, (\sigma, R), A_1, \ldots, A_n, bkg_1, \ldots, bkg_n$.

More precisely the procedure runs over the following steps:

1. It determines the "starting background" $bkg_1, \ldots, bkg_n$ for each profile fitting with a constant the external points of the profile (where it becomes flat). These values are used as input parameter for the backgrounds in the final fits.

2. It fits with a *King + bkg* function, providing $r_c, \alpha, bkg_1, \ldots, bkg_n$. If it exists, this fit is performed only to the non piled-up curve of the groups. Otherwise, it is performed on the curve with the smallest degree of pile-up. If the curve has no pile-up the determination of the r_c is quite accurate, otherwise if only piled-up measures are available, the core will be in any case uncertain.

3. It freezes r_c, α and fits all the curves of the group with *King + Gauss + bkg*, getting $\sigma, R, bkg_1, \ldots, bkg_n$. This hopefully provides some output parameters which are near to the best fit ones.

4. It thaws all the parameters and fits with *King + Gauss + bkg*. The output parameters of the previous step $r_c, \alpha, bkg_i, \sigma, R$ are used as initial input parameters for this final fit.

5. If the fit is "nonsense" (negative parameters or extremely large Gaussian parameters) the procedure is repeated with starting parameters obtained slightly shifting the previous ones. If, after 20 iterations, the fit is still nonsense, the procedure rejects the output values and fit the profile with *King+ bkg*.

The steps 2 and 3 are needed as the Gaussian component is quite small with respect to the King main component (also when the background is absent). Correspondingly, the initial guess of fitting parameters for the step 4 must be accurate. Such a sequence of steps successfully fine-tunes the input parameters in order to assure the fit convergence.

By applying this procedure to all the profiles, **I got that in no case the Gaussian component could be determined. In all the cases, the procedure adopted the "reduced" fit function *King + bkg*.** In fact, also in the best measures, the background is too high to distinguish the Gaussian component. The background value is roughly 10^{-4} times the King component (this is just a rough estimation, actually the background varies
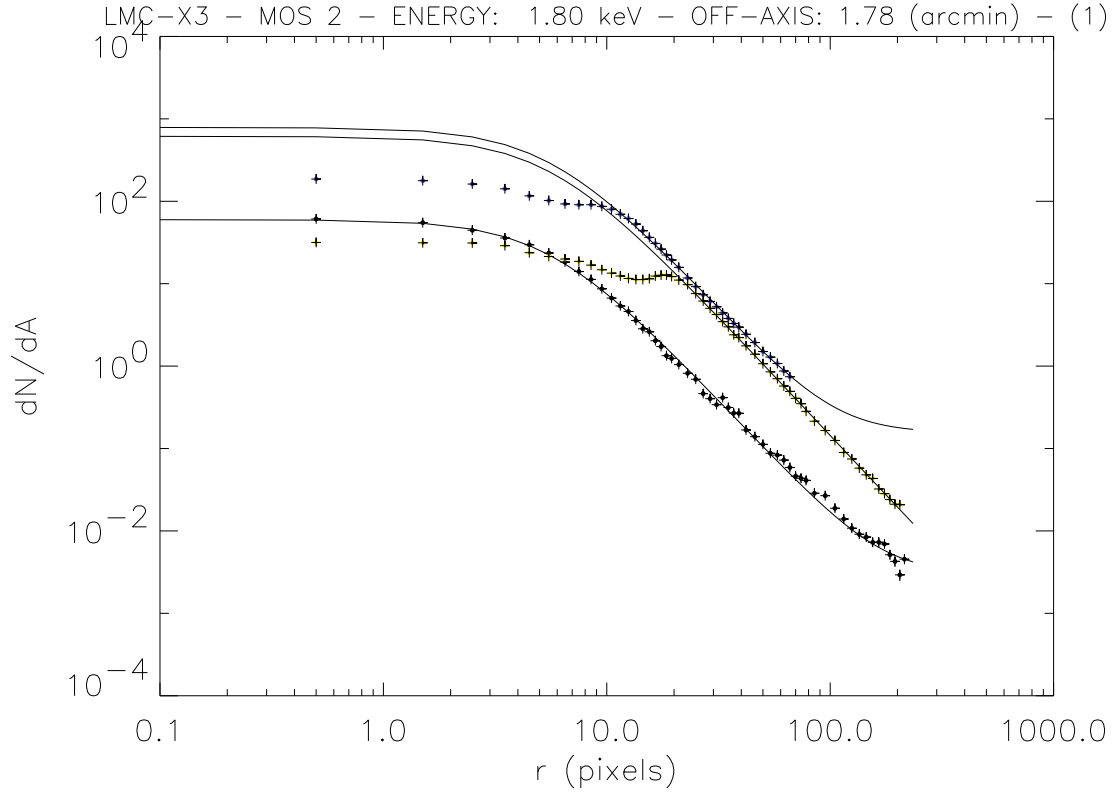
Figure 1: Simultaneous fit of three radial profiles having three different pile-up levels. The observations refer to LMC X-3 with an off-axis angle of 1.78 arcmin.The selected energy range corresponds to a mean energy of 1.8 keV.

measure by measure), which is of the same order of magnitude of the Gaussian component (from on-ground estimations) at $r \sim 100 - 150$ arcsec.

In Fig. 1, as an example, I report the simultaneous fit of three curves having three different pile-up levels. The source is LMC X-3. Data refer to MOS 2 camera. The energy range selected corresponds to a mean energy value of 1.8 keV. The off-axis angle is 1.78 arcmin. The three curves refers to

- Double Node with filter Thin: this corresponds to the black curve in figure with no pile-up effects;

- Large Window with filter Medium: this corresponds to the blue curve in the figure with some pile-up;

- Full Frame with filter Medium: this correspond to the yellow curve in the figure with the higher level of pile-up.

When fitting separately the three curves, the best fit parameters derived are (r_c is in arcsec):

$$r_c = 5.325 \pm 0.118,$$
$$\alpha = 1.423 \pm 1.389E - 02; \qquad (3)$$

for the first curve, using a fitting range of $[0.1 - 200]$ pixels (1 pixel=$1.1''$);

$$r_c = 6.238 \pm 4.244,$$
$$\alpha = 1.436 \pm 0.109; \qquad (4)$$

for the second curve, using a fitting range of $[20 - 230]$ pixels and

$$r_c = 9.028 \pm 1.618,$$
$$\alpha = 1.509 \pm 2.437E - 02; \qquad (5)$$

for the third curve, using a fitting range of $[30 - 230]$ pixels.

Using the simultaneous fitting procedure and adopting for each curve the same fitting range employed above:

$$r_c = 5.591 \pm 0.079,$$
$$\alpha = 1.449 \pm 0.006. \qquad (6)$$

As far as the core is concerned, only the first curve result (3) can be compared with the multi-fitting result (6), since the other two curves are affected by pile-up. The core of the first curve agrees within 2σ with the result obtained from the multi-fitting. Each slope parameter α obtained from the single fits (3-5) also agrees within 3σ with the result obtained with the multi-fitting; the multi-fitting procedure provides a result which is in agreement with all the single-fit results with the additional advantage of a reduced error on the best fit parameters thanks to the simultaneous use of the data points of the three profiles.

The same procedure has been applied to each group for each energy band. A set of best fit parameters (depending on energy and on off-axis angle) for each MOS has been derived.

3.2.3 The background

A crucial point for the fitting procedure is the determination of the background. Of course, an incorrect evaluation of the background can negatively affect the estimation of

the other best fit parameters. For example, an underestimation of the background leads to a best fit function with flatter wings as it tries to represent the plateau of the background. Hence, the fit returns a smaller slope parameter (α) and consequently a smaller core (r_c).

Two different methods can be adopted to evaluate the background. The first one consists in adding a background constant to the fit function (as already specified in the previous paragraphs). Another method consists in estimating the background in a "empty" region of the Field of View far away from the source. In this case, the radial profile is determined on the background subtracted image. The resulting profile is fit simply with a *King (+Gauss)* function.

Both methods present advantages and disadvantages. The main advantage in working on the background subtracted image is the reduction of the number of fitting variables (one *bkg* per each curve in the group). However, this method cannot be used on the stellar field (an "empty" region cannot be identified). Besides, the background must be corrected for the vignetting. The vignetting must be considered also when subtracting the background, considering that the radial profile extents out of about 4 arcmin from the centroid.

On the contrary, the evaluation of the background from a region away from the source can be useful when the source profile extension is not very large and the background estimation on the outer part of the wings is uncertain (or when Large/Small Window operating mode is used and wings are truncated before the flattening of the profile). In these cases the background from the fit with the *King + bkg* function is badly estimated.

In any case, the two methods can be combined to verify the goodness of the background estimation. In my analysis, I adopted the method which includes the background in the fitting function. However, I directly verified that for all the cases (when both methods could be used) the two methods provided values in agreement within 1-2 σ.

3.2.4   Good fitting range

When fitting a radial profile we must determine which points of the profiles must be used in the fitting procedure, i.e., a *good fitting range* must be defined. If the pile-up is absent the core can be easily evaluated, but often the statistics on the wings is poor. Therefore, it could be useful to reject the outer points and restrict the *good fitting range* for such a curve to the internal region. If some piled-up measure exists in the same group, it will supply the informations on the wings. Analogously, for a piled-up measure, the central points must be rejected and the *good fitting range* must be restricted to the external part of the profile. For each curve to be fitted, its *good fitting range* must be accurately determined.

Particular attention must be paid for those profiles which are slightly piled-up and it is not obvious where the pile-up starts reducing the counts. A wrong estimation of the *good fitting range* can lead to a biased result, since inclusion of piled-up points leads to an overestimation of the core radius.

First of all, I divided roughly the curves in four main groups: no pile-up, weak, strong and very strong pile-up. As a general rule, the following *good fitting range* can be adopted:

no pile-up   0.1 - 200,

weak   20 - 200,

strong   30 - 230,

very strong   40 -230,

(units are here in CCD pixels).

However, in most cases, some modifications are needed. Several methods have been adopted to correct these basic values.

If different pile-up levels are present in the same group, we can work as follows. We can plot the ratio between a profile and the profile with a smaller pile-up degree. The ratio will increase initially (where the two different pile-up levels differently affect the profile) and, moving towards the outer radii, finally the ratio should become flat, where pile-up does not affect the profiles any more. This flat range can be identified as the *good fitting range*.

When the simultaneous fit is not possible, e.g. for sources on the external CCDs, the *good fitting range* must be determined in a different way. By increasing the lower limit of the cutoff the output parameters can change significantly, as we progressively exclude part of the "damped" points. This effect fades progressively as we reach the point where the pile-up distortion is less important. The *good fitting range* is determined when the output fit parameters reach a "stationary" (within errors) behavior.

For GX13+1 observations, I could not find a *good fitting range*. As shown in the table below, moving the lower cutoff from $30''$ to $40''$ in the GX13+1 observation at 1.5 arcmin off-axis angle, at 1.8 keV, we find:

lower cutoff	r_c	σ_{r_c}	α	σ_α
$30''$	$5.49''$	$1.71''$	0.882	6.37E-03
$35''$	$4.51''$	$3.52''$	0.937	8.96E-03
$40''$	$4.61''$	$5.19''$	0.968	1.188E-02

Apart from the core (which is in any case unreliable for such a pile-up level), the α parameter continues to increase with the off-axis angle and the differences between the best fit values largely exceed 3σ. It is impossible to fix the lower limit for the *good fitting range* and, correspondingly, I rejected all those observations.

4 Results

The previously described procedures provide two sets (r_c and α) of best fit parameters corresponding to different selected energies and off-axis angles.

Before analyzing and modeling r_c and α, we can outline the expected behavior of both these shape parameters with the energy and the off-axis angles.

The core radius is expected to decrease when the energy increases, because the photons with higher energy will be reflected and focused only by the inner shells of the X–ray telescope. The reduced number of involved shells diminishes the source of "dispersion"; furthermore, the inner shells are probably less irregular. Both these effects improve the ability of focusing by the telescope with increasing energy.

Unlike the core, which becomes smaller when moving towards higher energies, the wings should become broader as energy increases. This is expected as high energy photons have a wavelength nearer to the roughness size of the telescope shells than low energy photons, with an enhanced probability of scattering processes. This effect gives prominence to the wings of the PSF, which become, for higher energies, more important. Consequently, the slope parameter α should decrease with increasing energy.

When moving off-axis, in general, the shape of the PSF will be distorted. Nevertheless, in this analysis we consider radially averaged profiles and the distortions are neglected. Moreover, for large off-axis angles, the telescope will lose ability of focusing and the PSF will be broadened; correspondingly the slope should decrease for increasing off-axis angles.

In the following paragraphs (§4.1 and §4.2), I will analyze the behavior of the core radius and of the slope versus energy and off-axis angle, respectively. In §4.3, instead, r_c and α are considered as 2-d functions of both energy and off-axis angles and an analytical modelization of these parameters will be provided. In §4.4, I will discuss the reliability of the final output model and I will define the *range of application*, i.e., those energies and off-axis angles for which the model can be applied. In §4.5, the Encircled Energy Fraction is studied, also for piled-up sources.

4.1 The core radius and the slope as a function of the energy

For each observation group, and, correspondingly, for each off-axis angle, we can derive the core radius and the slope as functions of the energy.

In Fig. 2, I plotted some examples of core radius versus energy, for MOS 1 (left column) and for MOS 2 (right column) at three different off-axis angles. The core radius is in arcsec and the energy is in keV.

As expected, the general trend of the core is to decrease as energy increases. Actually, when moving toward large off-axis angles, the number of points available is smaller, but in any case the trend holds.

We can also observe that a linear behavior with the energy could be a fair modelization of the core trend. The line overplotted in the graphs *is not* the best fit, but the result of a 2-d fit which will be introduced and widely discussed in §4.3.

Analogously, in Fig. 3, I plotted the slope (α) versus energy (in keV) for some off-axis angles. The dependence of α on the energy is small. There is a slight tendency to decrease (as expected) when energy increases. Like for the core radius, also α can be well represented as a linear function of the energy. The fit overplotted is again the result of the 2-d fit discussed in §4.3.

4.2 The core radius and the slope as a function of the off-axis angle

For each energy, we can consider all the different observations corresponding to different off-axis angles and we can plot the core radius and the slope as functions of the off-axis angle.

In Fig. 4, I plotted, for the energies 1, 3.7, 6.5 keV, the core radius (in arcsec) versus the off-axis angle (in arcmin). The left column refers to MOS 1 data and the right column to MOS 2 data. Data are quite scattered and the large off-axis angles are no longer sampled when considering high energies. For small energies, where measurements at large off-axis positions are available, the core does not show a significant variation for increasing off-axis angles. When considering higher energies, few points are available for large off-axis angles, and in general they have a large error bar. Points show a slightly decreasing trend, but a constant behavior can match as well. The reliability of the modelization for these off-axis angles and energies will be discussed widely in §4.4. Note that the solid lines are not here the best fits, but they have been obtained by means of the 2-d fit described in §4.3. A linear trend can be used to model the core behavior.

In Fig. 5, the slopes vs. off-axis angle (arcmin) are plotted for the energies 1.0, 3.7
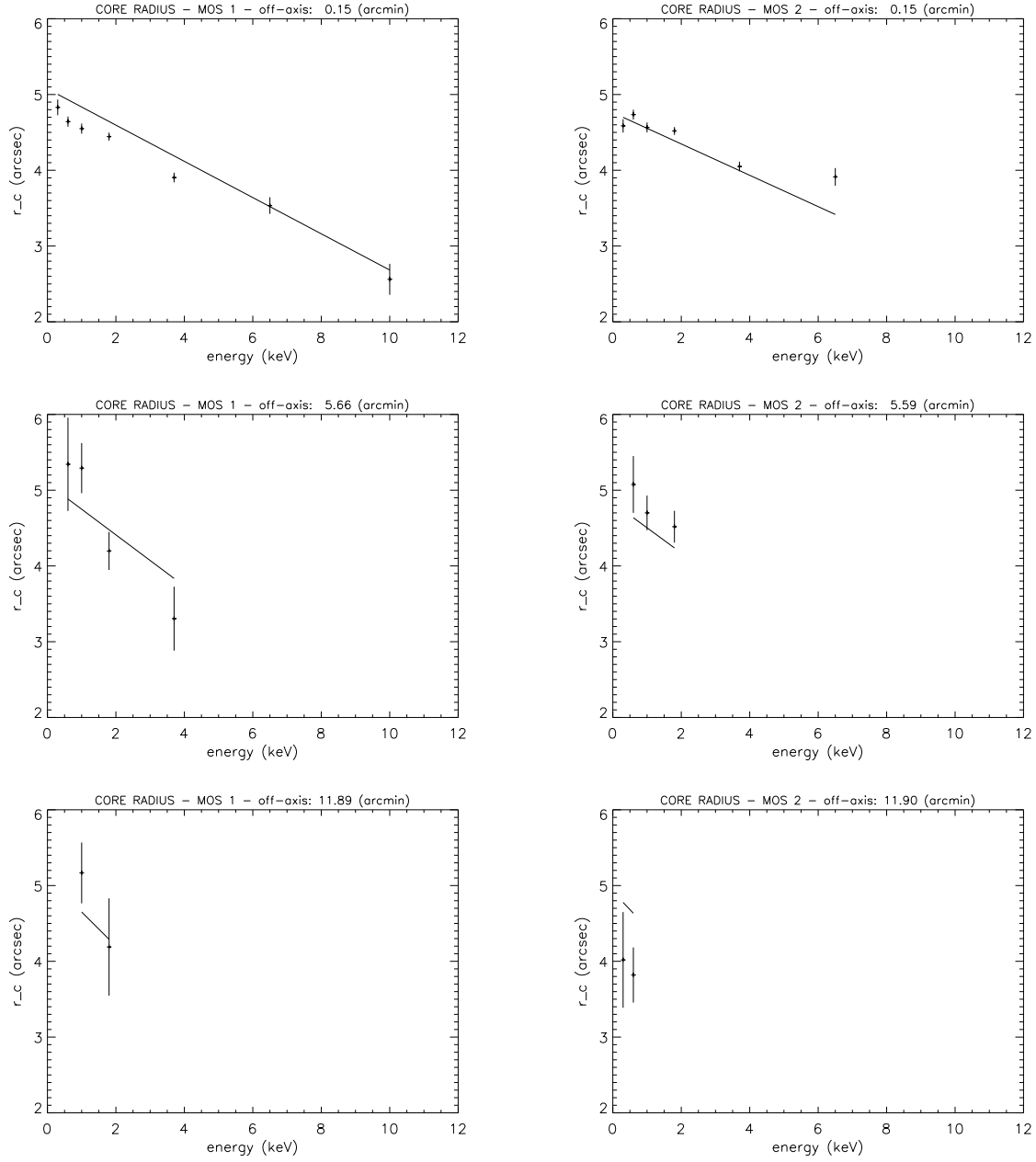
Figure 2: King core radius (arcsec) vs. energy for some off-axis angles. Left column refers to MOS 1 observations and right column to MOS 2. The solid lines refer to a 2-d fit (see §4.3).
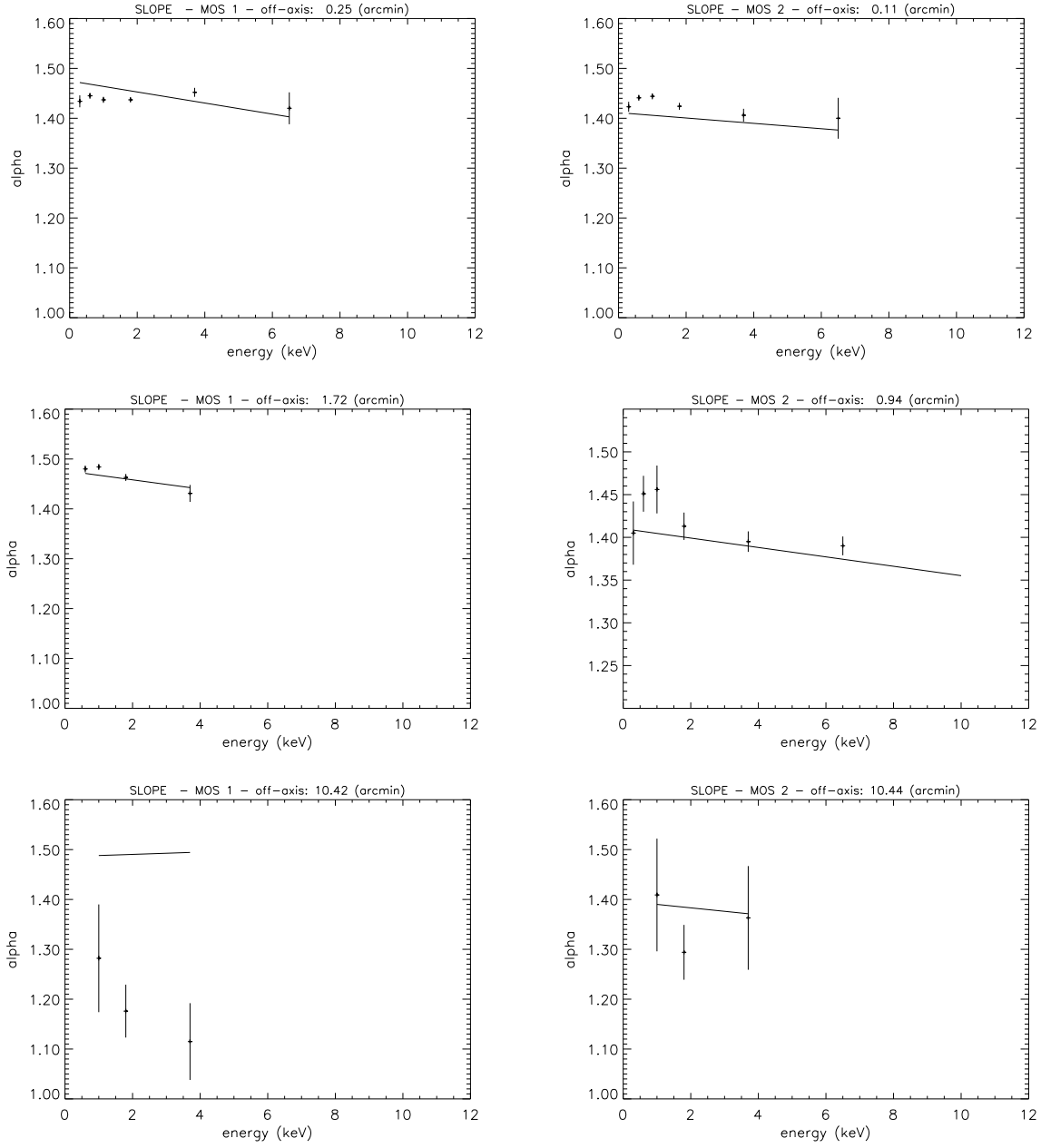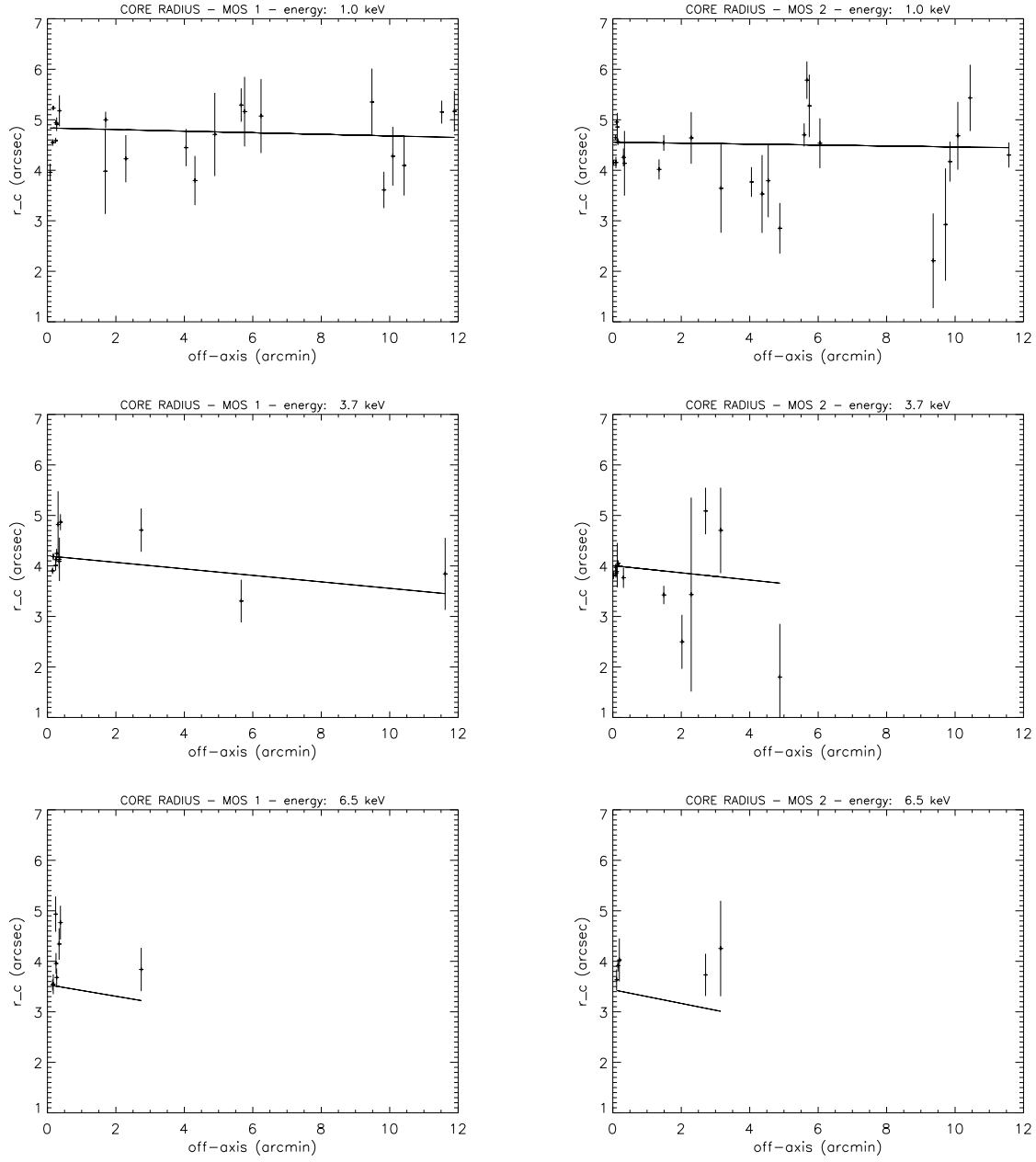
Figure 3: King slope vs. energy for some off-axis angles. Left column refers to MOS 1 observations and right column to MOS 2. The solid lines refer to a 2-d fit (see §4.3).

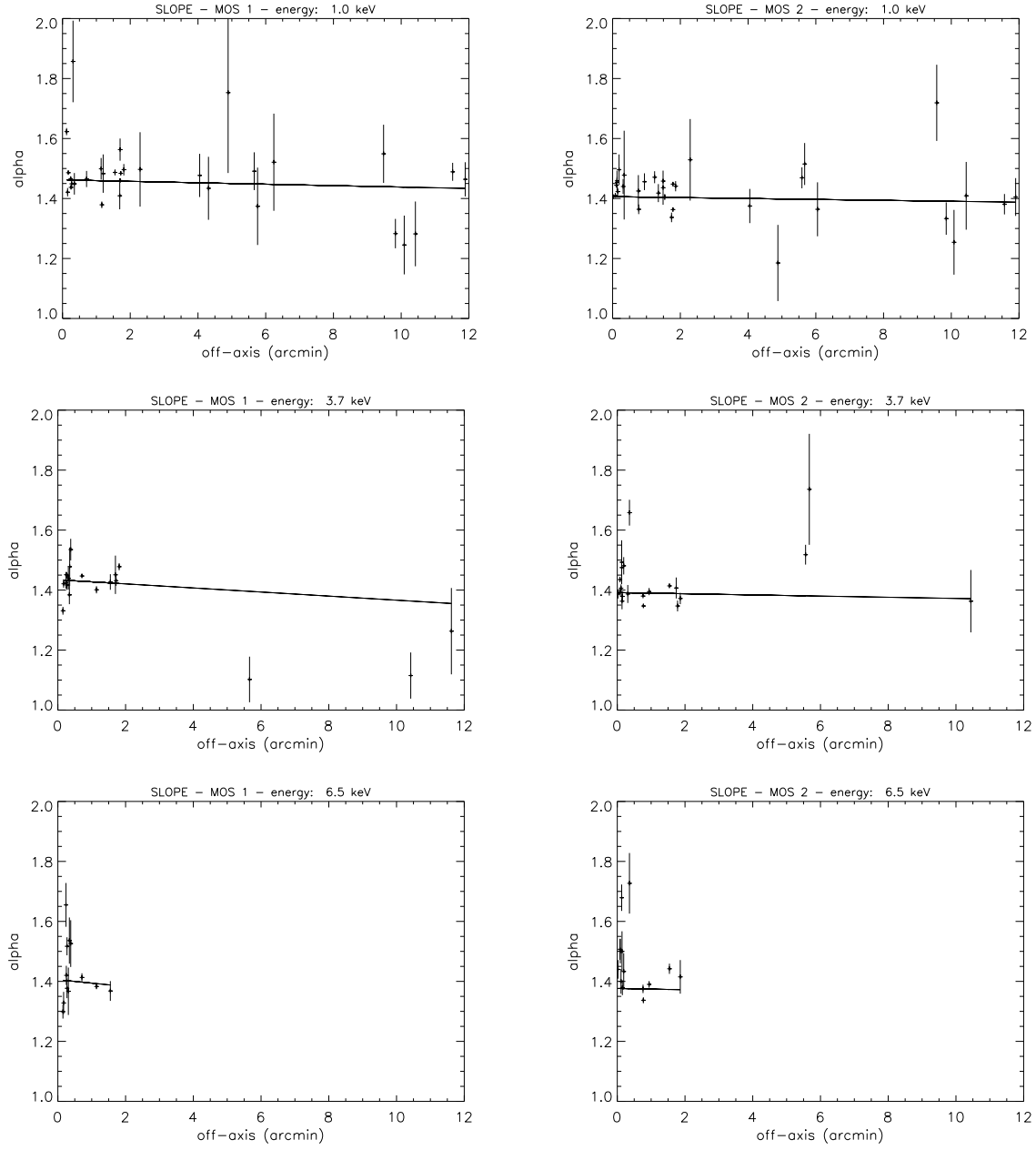Figure 4: King core radius (arcsec) vs. off-axis angle (arcmin) for 1., 3.7 and 6.5 keV. Left column refers to MOS 1 observations and right column to MOS 2. The solid lines refer to a 2-d fit (see §4.3).

Figure 5: King slope vs. off-axis angle (arcmin) for 1., 3.7 and 6.5 keV. Left column refers to MOS 1 observations and right column to MOS 2. The solid lines refer to a 2-d fit (see §4.3).

and 6.5 keV (left column: MOS 1; right column: MOS 2). The slope shows a decreasing behavior for increasing off-axis angles, which is more pronounced for higher energies. The error bars for the slopes are smaller than those for the core radius, but again points at high energies and large off-axis angles are not sampled. In the panel corresponding to 3.7 keV energy, the points at large off-axis angles have large error bars if compared to the other points in the plot. These points refer to some stars in OMC2/3, where actually the slope is not really well sampled. See §4.4 for a discussion on the reliability of the model in these points.

Again, we can see that a linear trend is suitable for describing the behavior of the slope for each energy as a function of the off-axis angle.

In general, we can infer that the core and the slope don't show any significant variation with the off-axis angle, at low energies. At larger energies, a decreasing trend holds for both the shape parameters but, as will be discussed in §4.4 for these energies, the modelization concerns only nearly on-axis positions.

4.3 The King core radius and the slope as functions of energy and off-axis angle

Rather than fitting separately with linear functions, it is worth to consider r_c and α as 2-d functions of energy and off-axis angles.

According to Figs. $2-5$, we can conclude that, whenever one of the two independent variables (energy or off-axis angle) is fixed, r_c and α vary roughly linearly with the other variable. More precisely:

$$\frac{\partial r_c}{\partial E}\bigg|_\Theta = A = constant,$$

$$\frac{\partial r_c}{\partial \Theta}\bigg|_E = B = constant.$$

being E the energy and Θ the off-axis angle. Similar equations are valid for α. By means of simple integrations, it can be seen that

$$r_c(E, \Theta) = a + b \cdot E + c \cdot \Theta + d \cdot E \cdot \Theta, \tag{7}$$

and analogously

$$\alpha(E, \Theta) = x + y \cdot E + z \cdot \Theta + w \cdot E \cdot \Theta. \tag{8}$$

Fitting the available set of r_c and α with eqs. (7) and (8), we obtained the values reported in Table 1:

Table 1: r_c and α best fit according to eqns. (7) and (8)

	MOS 1			
r_c	$a = 5.074 \pm 0.001$	$b = -0.236 \pm 0.001$	$c = 0.002 \pm 0.001$	$d = -0.0180 \pm 0.0006$
α	$x = 1.472 \pm 0.003$	$y = -0.010 \pm 0.001$	$z = -0.001 \pm 0.002$	$w = -0.0016 \pm 0.0013$
	MOS 2			
r_c	$a = 4.759 \pm 0.018$	$b = -0.203 \pm 0.010$	$c = 0.014 \pm 0.017$	$d = -0.0229 \pm 0.0133$
α	$x = 1.411 \pm 0.001$	$y = -0.005 \pm 0.001$	$z = -0.001 \pm 0.002$	$w = -0.0002 \pm 0.0011$

The fit has been performed considering the energy in keV units and the off-axis angles in arcmin units; r_c is in arcsec. The coefficients a and x give the order of magnitude of r_c and α respectively. The other coefficients give the variations with energy and off-axis positions.

In Figs. 6–9 we draw the parameters r_c and α in a 3-d plot and in a contour plot. It can be seen that the variations of α are quite small. For each off-axis angles, α is decreasing with the energy, and, if an energy is fixed, α decreases for increasing off-axis angles. However, it is worth to notice that the variations are always modest.

From Table 1 and Figs. 7 and 9, we can see that the slope of the MOS 2 PSF is smaller than the slope of the MOS 1 PSF.

The core radius shows a similar behavior for the two MOS cameras. The MOS 2 PSF has a slightly smaller core radius with respect the MOS 1 PSF.

Once r_c and α have been obtained, each radial profile determined with the algorithms described in Section 3, can be fitted with a *King + bkg* function, where the core and the slope are fixed according to the selected energy and the off-axis angle of the profile.

In Figs. 10 and 11, I plot, as an example, the profiles of some observations (with different pile-up levels) with the final *King + bkg* best fit, where only the total normalization and the background have been retained as free parameters.

In Fig. 10, concerning three observations of LMC X-3 (at 1. keV nearly on-axis), it can be seen that the best fit matches the data points very well. In Fig. 11, we plotted some profiles of HR1099 (at 1 keV, nearly on-axis). In this case, there are only piled-up profiles. However, also in this case, the slope matches the data and also the fit of the core seems suitable.
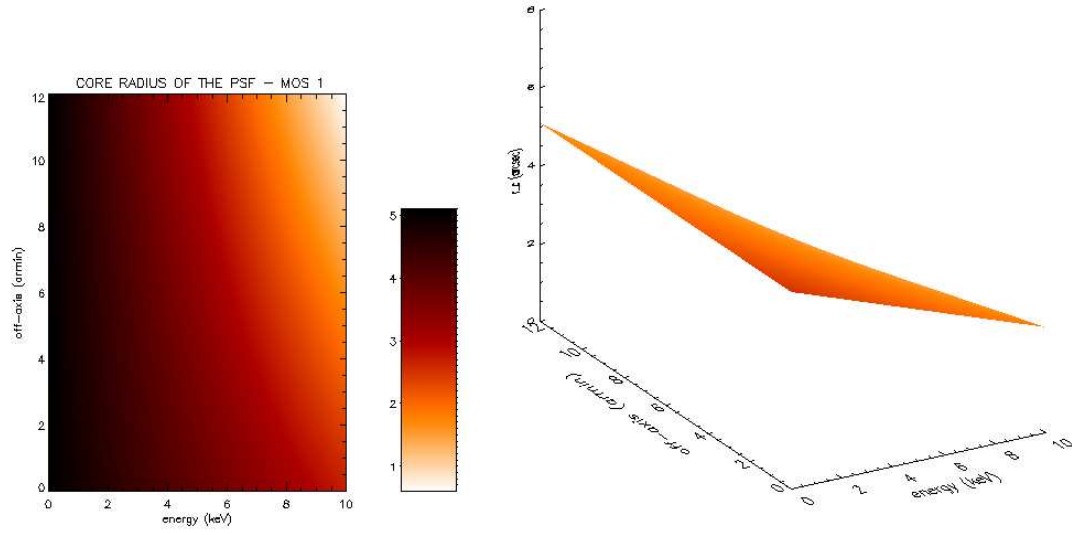
Figure 6: King core radius as a function of the off-axis angle and energy for MOS 1.
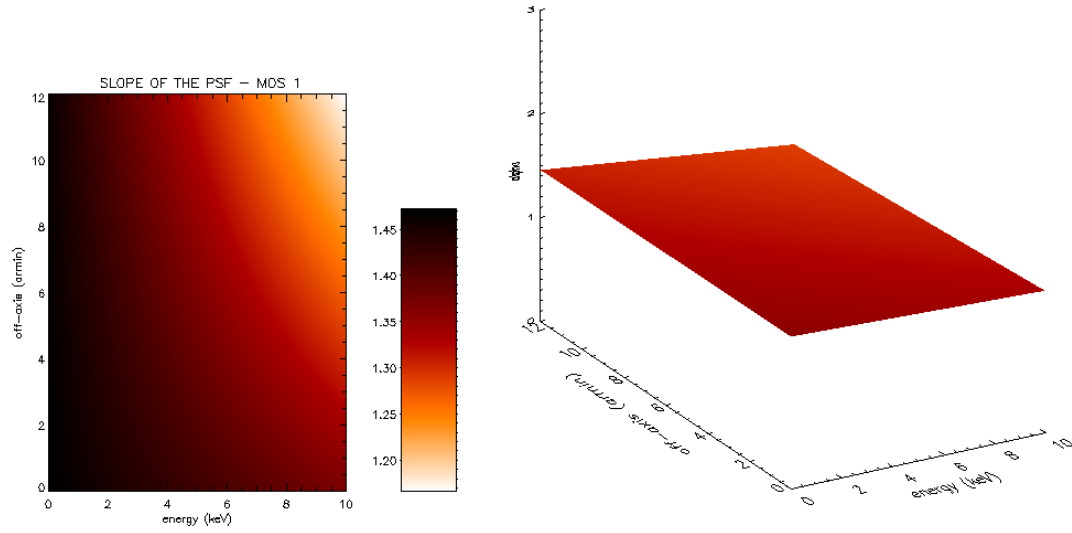

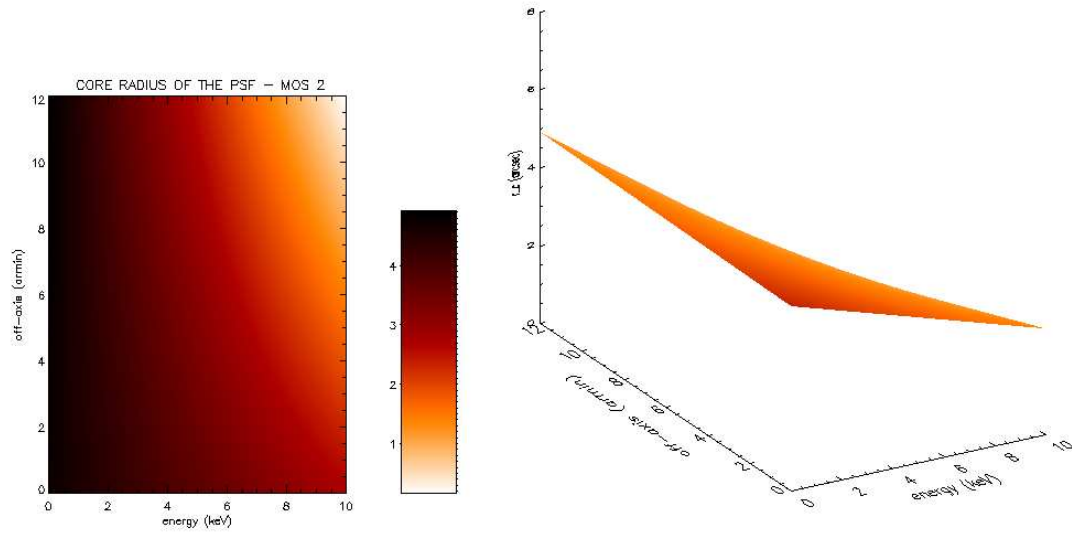Figure 7: King slope as a function of the off-axis angle and energy for MOS 1.

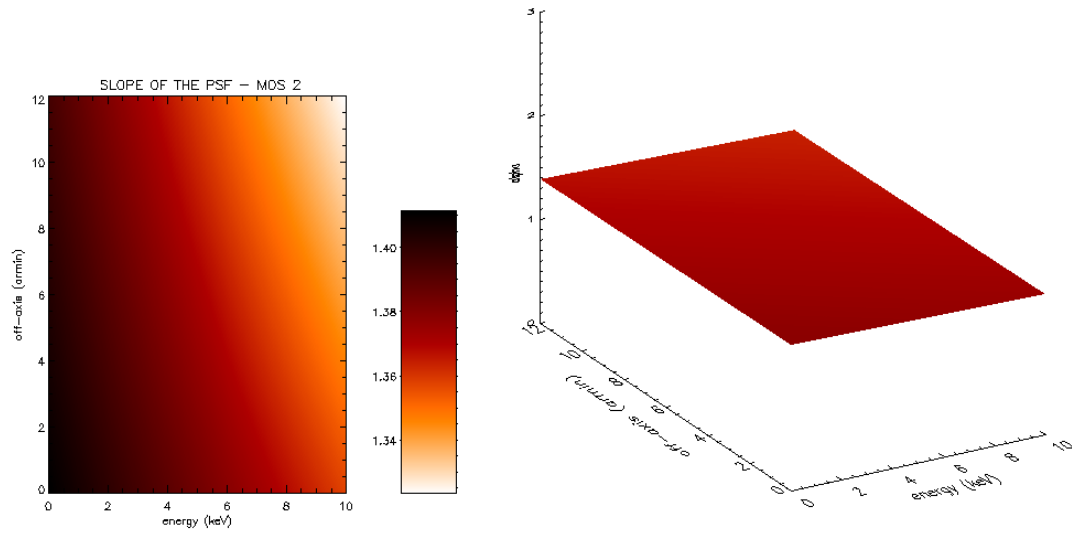Figure 8: King core radius as a function of the off-axis angle and energy for MOS 2.

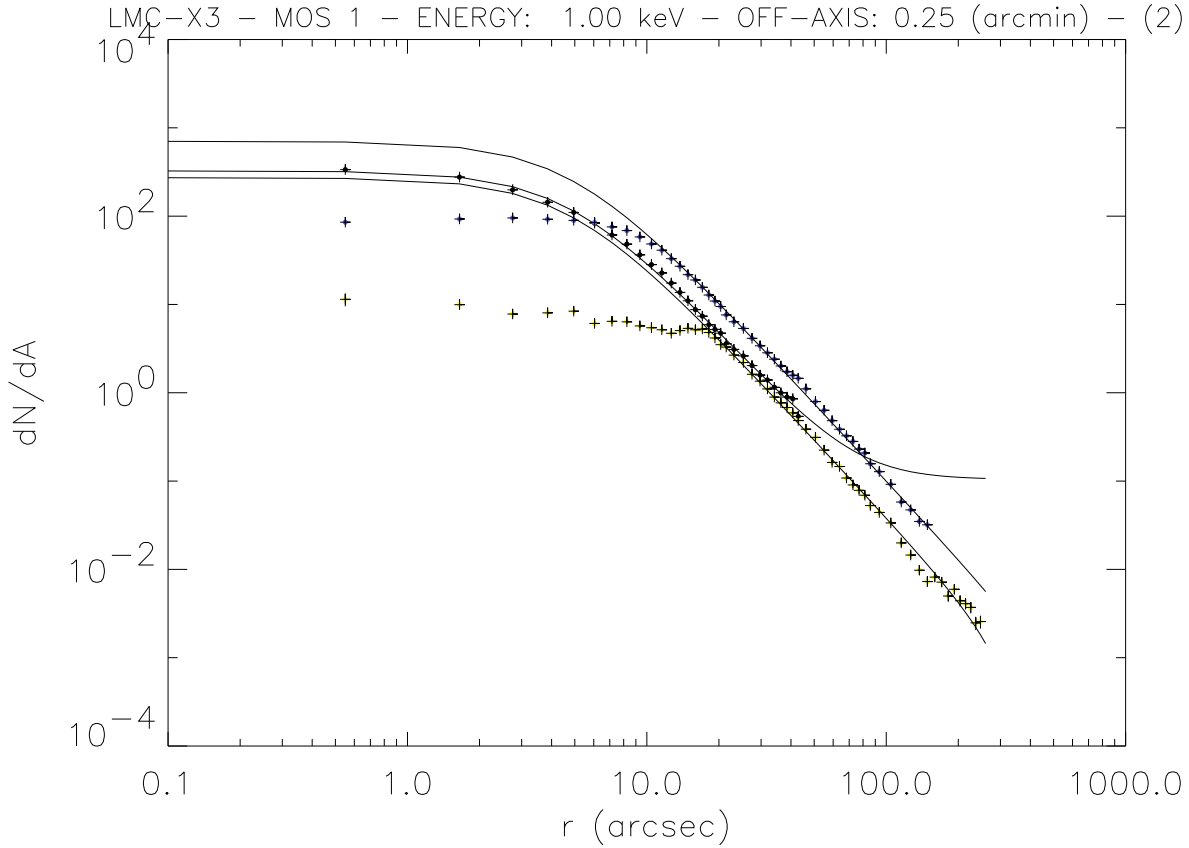Figure 9: King slope as a function of the off-axis angle and energy for MOS 2.

Figure 10: Data referring to observations of LMC X-3 at 0.25 arcmin off-axis position. Solid lines are the fits with r_c and α are fixed according to the Table 1.

4.4 Reliability of final output model.

As previously outlined, Figs. 2–5 show that, when moving toward large off-axis angles, the data available are reduced and in general (because of the small effective area at high energies) the points corresponding to high energies (say $\gtrsim 5\,\mathrm{keV}$) disappear. As a matter of fact, no informations are available at high off-axis angles and high energies, hence **the calibration for these regions is not available**.

In Figs. 12–15, I plotted the same figures as Figs. 6–9 with the sample data points marked on. The eqns. (7) and (8) with values listed in Table 1 are valid only within regions covered by asterisks in Figs. 12–15. The regions covered by the asterisks define the **range of application** of the model. **The high energy and high off-axis angle region (top-right part of the plot) is excluded from the *range of application*. The model cannot be used there.**

25
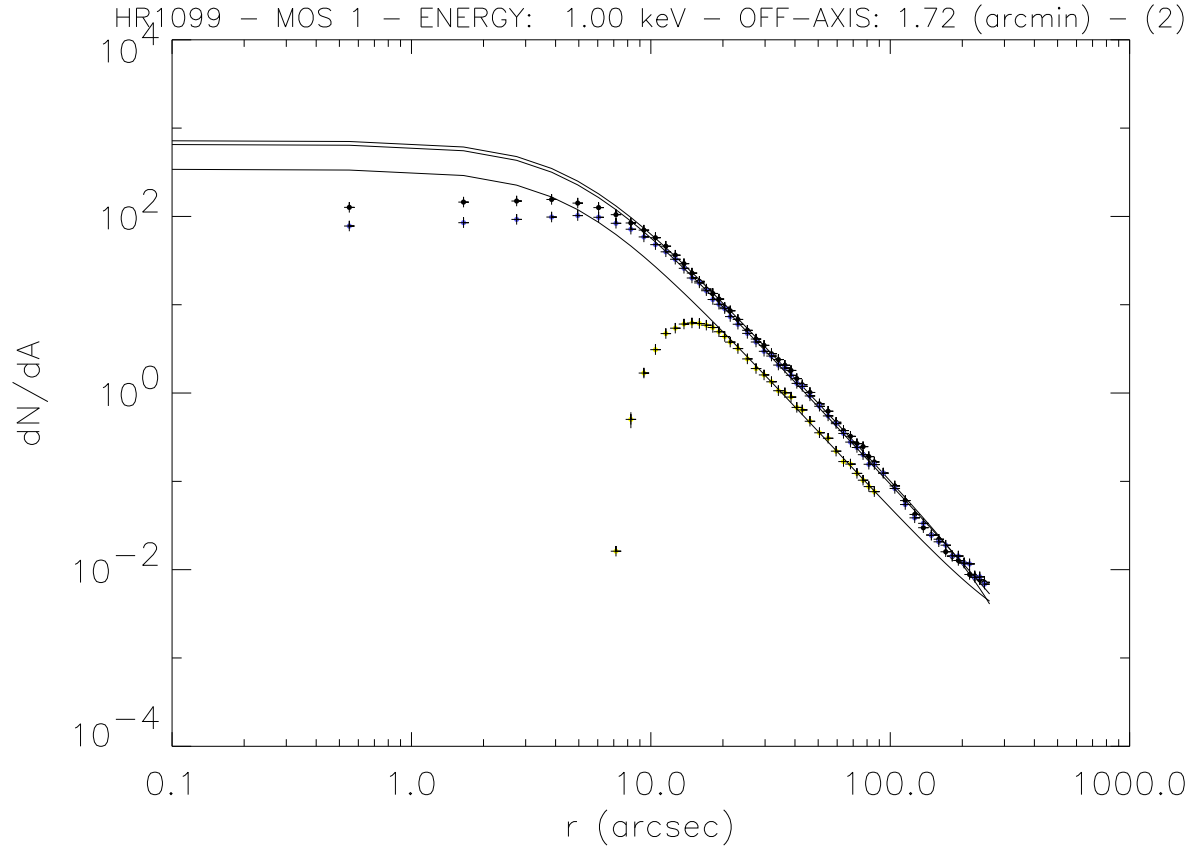
Figure 11: Data referring to observations of HR1099 at 1.72 arcmin off-axis position. Solid lines are the fits with r_c and α are fixed according to the Table 1.
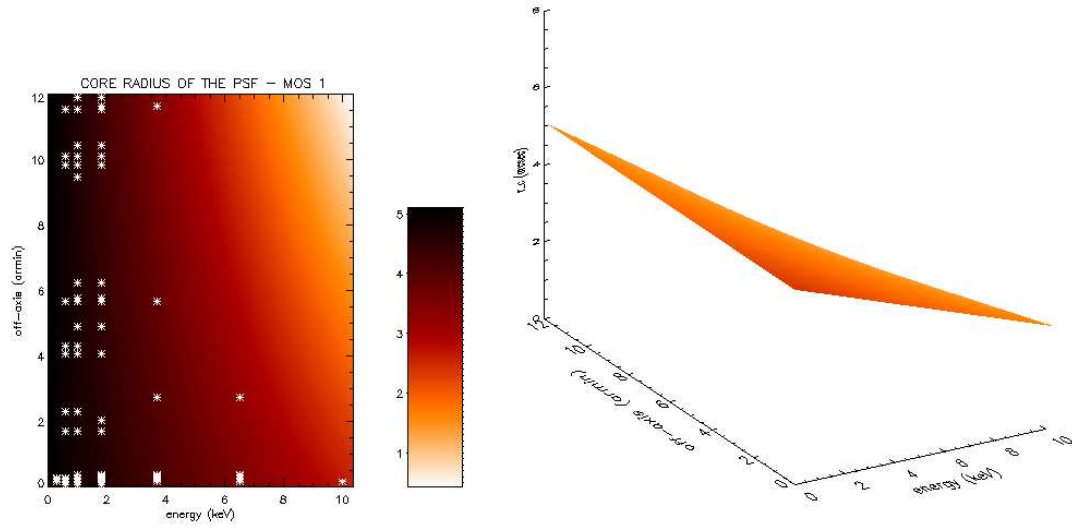
Figure 12: King core radius as a function of the off-axis angle and energy for MOS 1. Superimposed crosses correspond to measured data points.
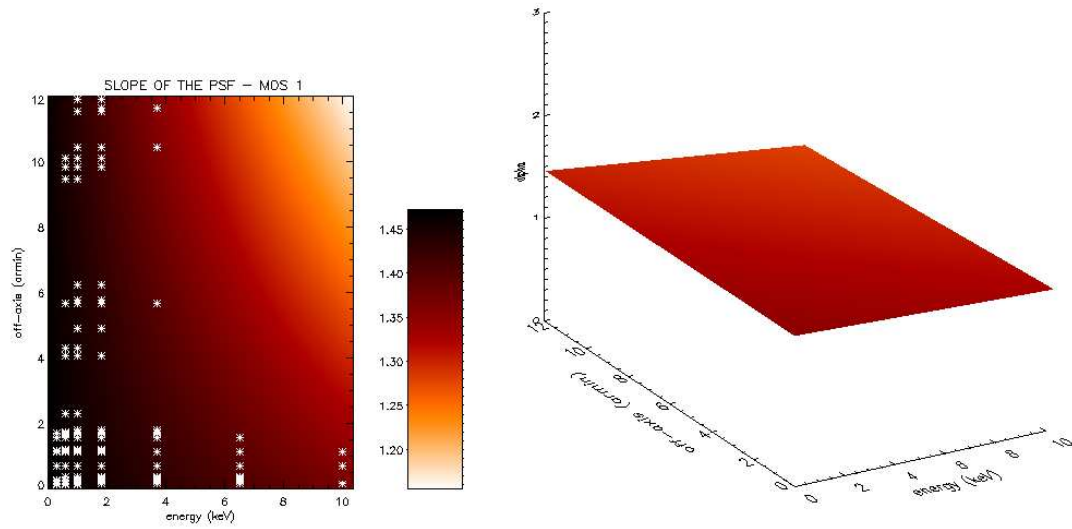

Figure 13: King slope as a function of the off-axis angle and energy for MOS 1. Superimposed crosses correspond to measured data points.
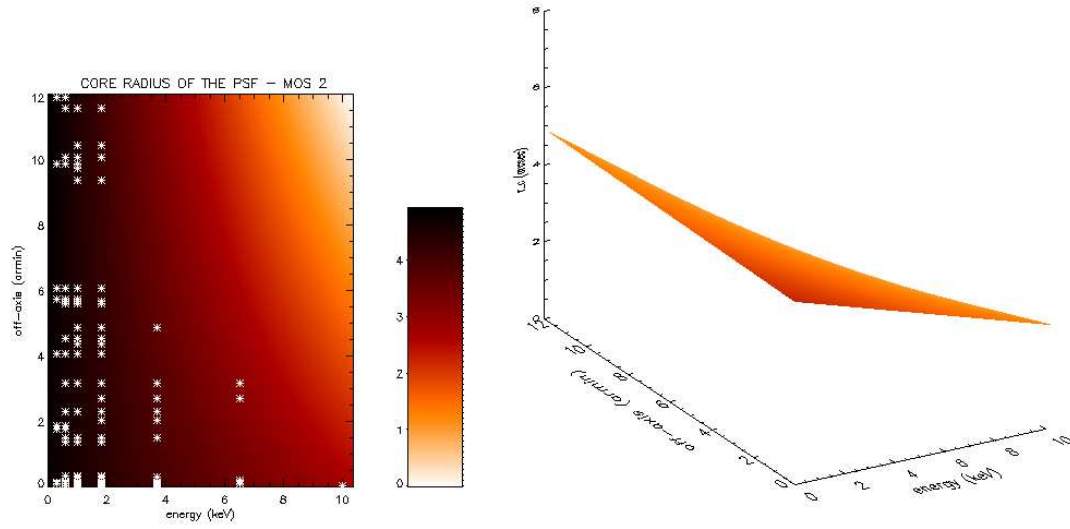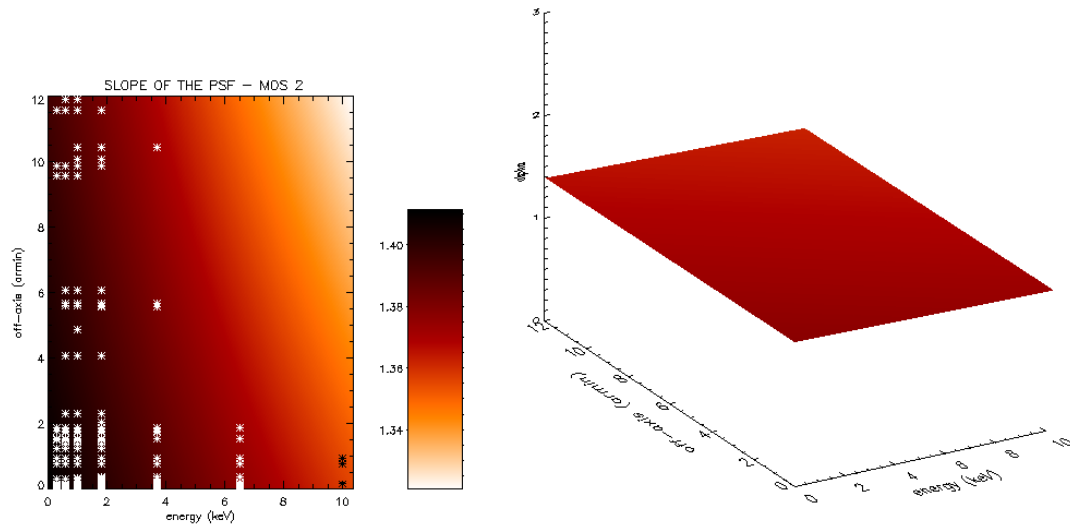
Figure 14: King core radius as a function of the off-axis angle and energy for MOS 2. Superimposed crosses correspond to measured data points.

Figure 15: King slope as a function of the off-axis angle and energy for MOS 2. Superimposed crosses correspond to measured data points.

Apart from the region where points are missing, some problems arise also at intermediate off-axis angles ($\sim 5'$) where points are available but have also large errors and they do not constraint significantly the modelization of the PSF. Often points at large off-axis angles refer to stars in the field OMC2/3, or some small sources which are present in the field of view (referred in Table 3 as LMC2, Capella2 or sources in HCG016) whose statistic is not very high. In Fig. 16 we report an example for an $11.57'$ off-axis image of a source in HCG016 at 1.8 keV. It can be seen that the core and the slope can be determined with a quite large error. In Fig. 17 we report the profile at $\sim 5'$ off -axis for 3.7 keV, for a star in OMC2/3. Again, it can be seen that the statistic is not very high and because of the high background, only points within 45 pixels ($\sim 50''$) are retained. The measure is uncertain and the best fit parameters have a large error bar (see figs. 4–5). These points give an uncertain modelization of the final PSF. So the King function with coefficient given in eqns. (7) and (8) and Table 1 must be used for these values with caution.

In Fig. 18 we divided the space energy–off-axis angles in three regions. The modelization of the PSF in the region marked in green is safe. A large set of well sampled points is available and the inferred parameters are reliable. The modelization cannot be used for values belonging to the red region: no calibration points are there available. For points belonging to the yellow regions the modelization must be used with caution. Calibration points for these regions have large error bars and the calibration is uncertain. More calibration sources must be observed in these regions to obtain a more precise evaluation of the parameters. Note that the regions at low energies (~ 1 keV) are green, even if the error bars of the points are large (see for example, the panels in figs. 4 and 5 corresponding to 1 keV). Although the points at large off-axis angles have large errors and are rather scattered around the best fit line, there are a lot of measures; hence the modelization is good.

Note: two different colors in Figs. 12–15 have been used for the crosses only to distinguish them from the background colors.

4.5   Encircled Energy Fraction

An important quantity characterizing the PSF is the Encircled Energy Fraction, which specifies the fraction f of energy collected within a certain radius R.

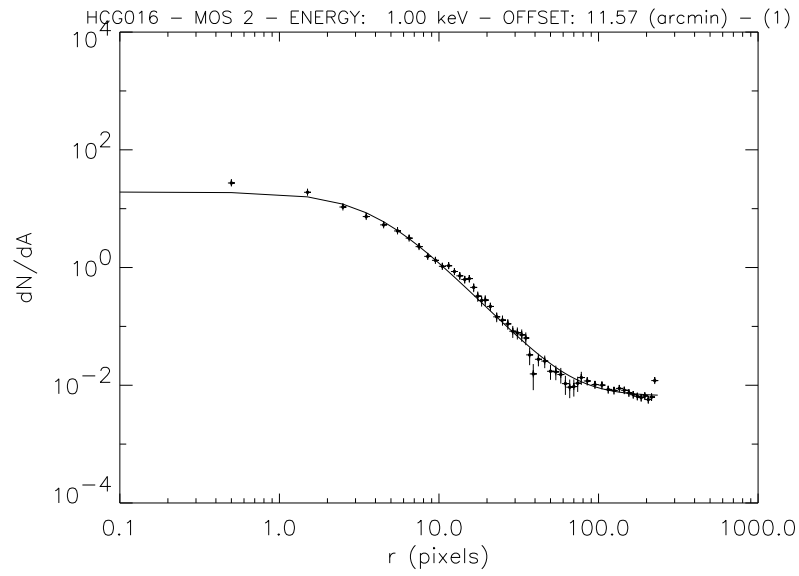This quantity is defined according to:

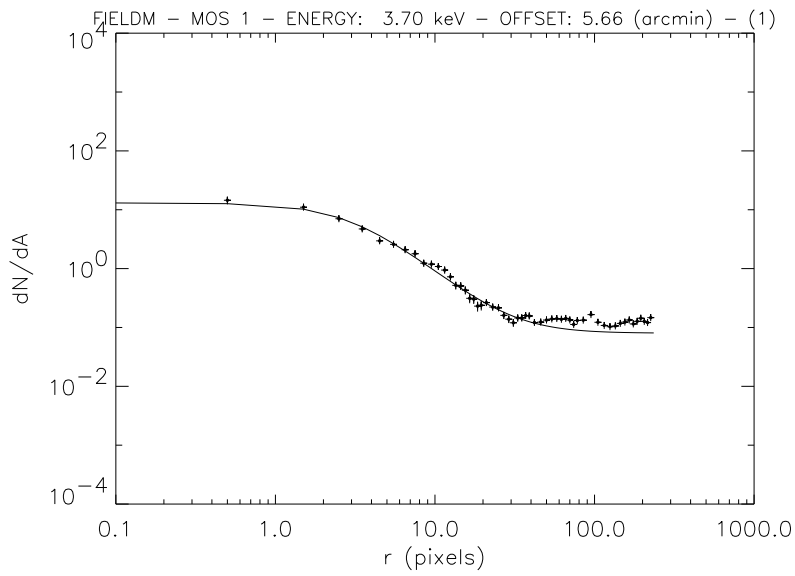Figure 16: Profile of a point source in HCG016.

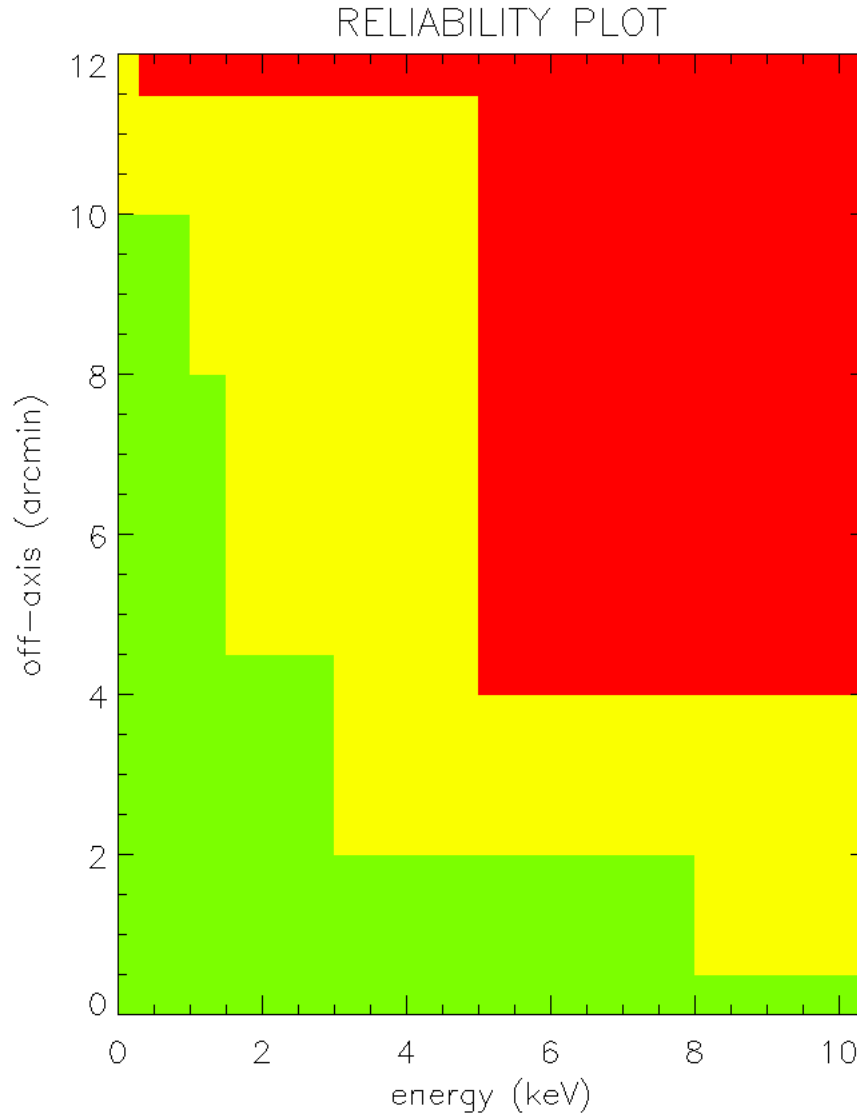Figure 17: Profile of a star in OMC2/3 field.

Figure 18: Plot showing the reliability of the modelization of the PSF. The red region marks the points for which calibration measures are not available and correspondingly there is no calibration. The green region corresponds to those energies and off-axis angles for which the calibration is well-sampled and the modelization provides a good description of the PSF. The yellow region covers the points for which data have large errors and the modelization is uncertain. The modeled PSF in these regions must be used with caution.

$$EEF(R) = \frac{\int_0^R PSF(r)rdr}{\int_0^{R_N} PSF(r)rdr} \; .$$

R_N defines the total normalization. If we assume that the King profile holds to infinity then $R_N = \infty$. Actually data profiles never go beyond 5 arcmin. Therefore, for larger radii, the modelization of the PSF profile is impossible, also because of the background which becomes important and hides other possible components of the PSF (e.g. the Gaussian component that we saw in the ground calibration data). For this reason, we decide to fix $R_N = 5$ arcmin. Using the King function (see eqn. (2)),

$$EEF(R) = \frac{\int_0^R \frac{1}{\left[1 + \left(\frac{r}{r_c}\right)^2\right]^\alpha} rdr}{\int_0^{5'} \frac{1}{\left[1 + \left(\frac{r}{r_c}\right)^2\right]^\alpha} rdr} \; . \tag{9}$$

This quantity can be easily integrated and EEF can be written as follows:

$$EEF(R) = \frac{1 - \frac{1}{\left[1 + \left(\frac{R}{r_c}\right)^2\right]^{\alpha-1}}}{1 - \frac{1}{\left[1 + \left(\frac{5'}{r_c}\right)^2\right]^{\alpha-1}}} = f \; . \tag{10}$$

We can compare the results on the EEF when using $R_N = 5$ arcmin and $R_N = \infty$ (which is the largest possible radius). f we measure a flux $F_{meas.}$ within a radius R the total flux F_{TOT} within R_N is, by definition:

$$F_{TOT}^{R_N} = \frac{F_{meas.}}{f(R)} \; .$$

We can compare $F_{TOT}^{5'}$ and F_{TOT}^{∞}:

$$\frac{F_{TOT}^{5'}(R)}{F_{TOT}^{\infty}(R)} = \frac{f^{R_N=\infty}}{f^{R_N=5'}} = 1 - \frac{1}{\left[1 + \left(\frac{5'}{r_c}\right)^2\right]^{\alpha-1}} \; .$$

The two parameters r_c and α are given in eqns. (7) and (8) and in Table 1. Note that the ratio does not depend on the radius R.
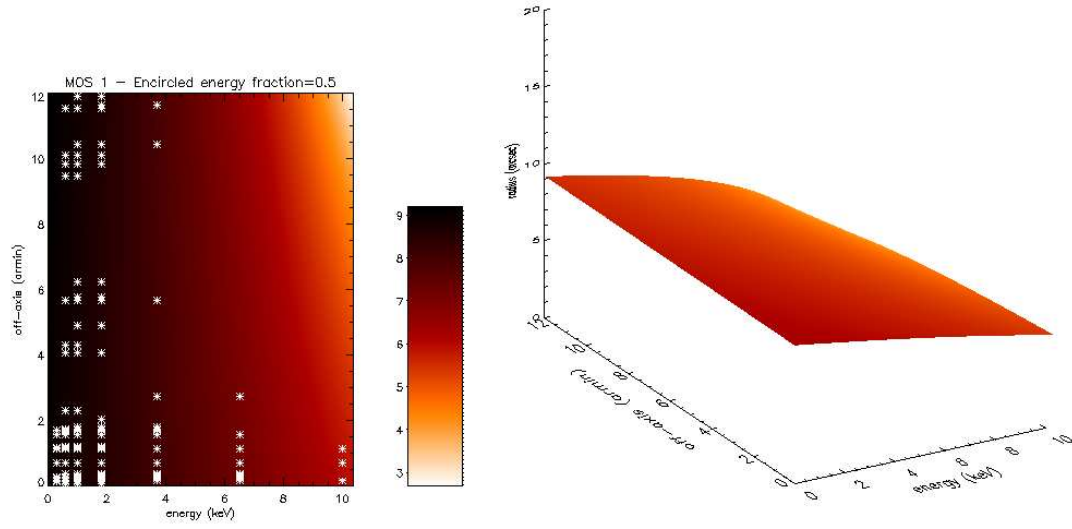
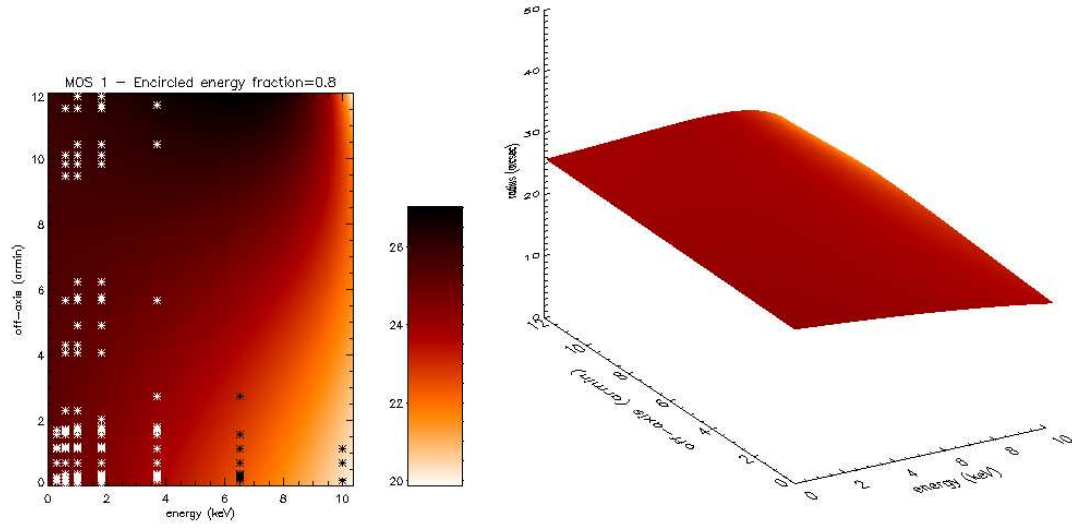Figure 19: Radius enclosing 50% of energy (arcsec units) for MOS 1.

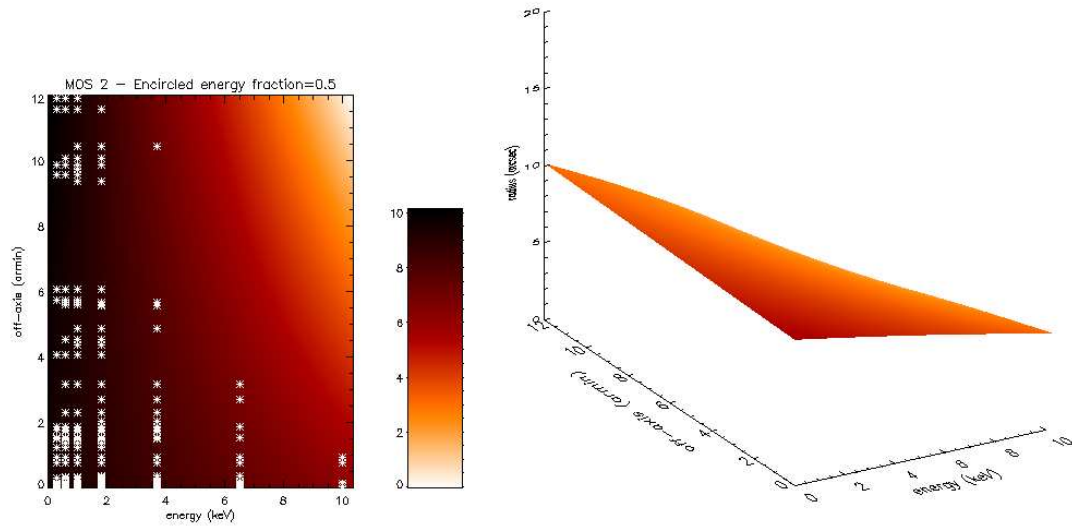Figure 20: Radius enclosing 80% of energy (arcsec units) for MOS 1.

33

Figure 21: Radius enclosing 50% of energy (arcsec units) for MOS 2.
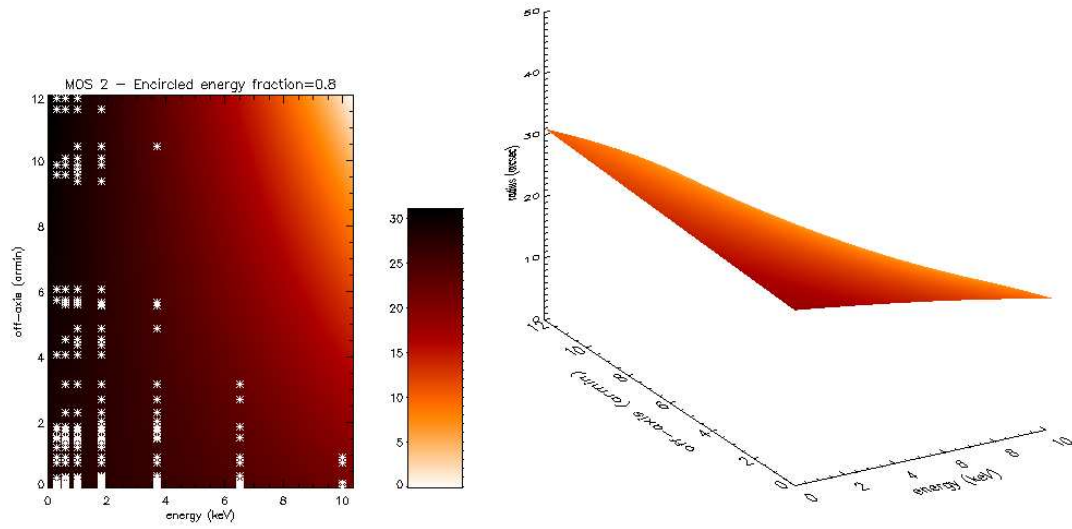

Figure 22: Radius enclosing 80% of energy (arcsec units) for MOS 2.

For the MOS 1 camera, the ratio hereabove varies from 0.965 to 0.985 within the *range of application* defined in §4.4, and for the MOS 2 it varies from 0.960 to 0.967. On the whole, the difference between the two estimations is of the order of 2-4%.

Starting from eqn. (10), we can easily derive the radius R at which a fraction f of energy is encircled.

$$R(f; r_c, \alpha) = r_c \left\{ \left[1 - f \left(1 - \frac{1}{\left[1 + \left(\frac{5'}{r_c} \right)^2 \right]^{\alpha - 1}} \right) \right]^{\frac{1}{1 - \alpha}} - 1 \right\}^{\frac{1}{2}} . \tag{11}$$

In Figs. 19 − 22, we show the radii enclosing 50% and 80% of the energy, for MOS 1 and MOS 2. Considering that α is roughly constant with energy and off-axis angles, the main behavior of R is similar to that of r_c. Note that, like the PSF, the EEF defined in eqn. (10) is valid only within the range of application introduced in §4.4 and represented in fig. 18.

In Figs. 23–26, we show the radius enclosing 50% and 80% of the total energy, for the on-axis position, for MOS 1 and MOS 2. The radius is plotted in arcsec unit. Superimposed crosses refers to the data set. The ***range of application*** described in §4.4 and represented in Fig. 18 must be accounted.

At low energies, $R(50\%)$ is $\sim 9''$ for MOS 1 and slightly larger ($\sim 9.5''$) for MOS 2. R decreases with energy and, at 10 keV, $R(50\%)$ is $\sim 6.3''$, for both the MOS cameras.

Analogously, $R(80\%)$ is $\sim 25''$ and $\sim 29.5''$ for MOS 1 and MOS 2 respectively. At high energies, $R(80\%)$ goes to $\simeq 21''$ for both the cameras.

In Table 2 the values of $R(50\%)$ and $R(80\%)$ are reported for the energies 1.5, 8, 9 keV, for MOS 1 and MOS 2.

4.5.1 EEF for piled-up sources.

For piled-up sources the central part of the profile of the PSF is damped and it can be completely missing if the pile-up is very strong. In these cases, a different definition of the EEF could be useful. A lower cutoff R_L in eqn. (9) can be added in order to exclude the inner points. R_L can be chosen according to the pile-up level of the observation.

Accordingly, the energy fraction EEF enclosed in the annulus $[R_L - R]$ can be written:
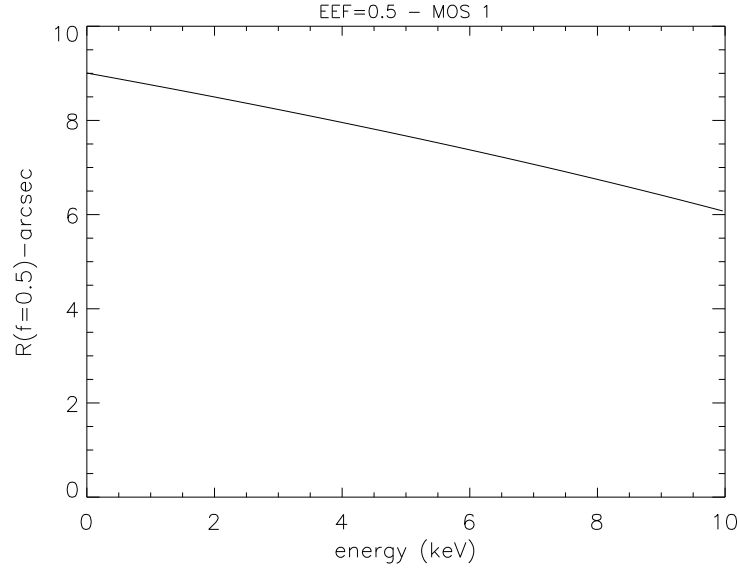
Figure 23: Radius enclosing 50% of energy (arcsec units) for the on-axis position for MOS 1.
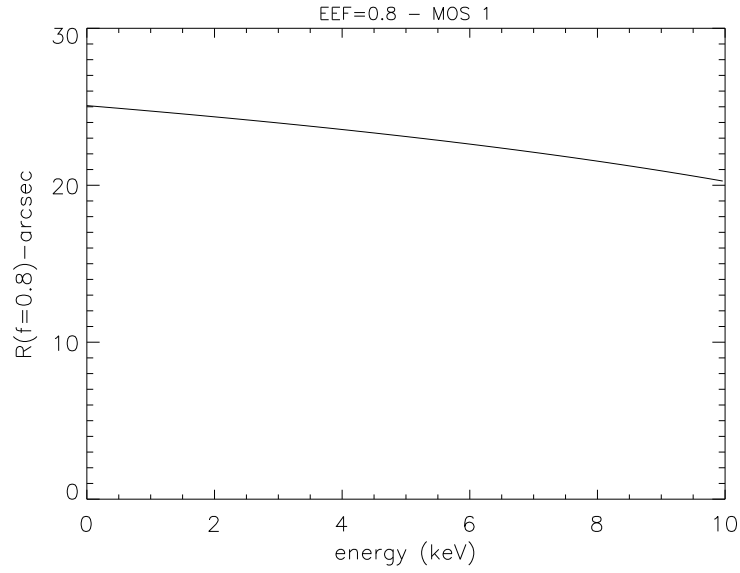

Figure 24: Radius enclosing 80% of energy (arcsec units) for the on-axis position for MOS 1.
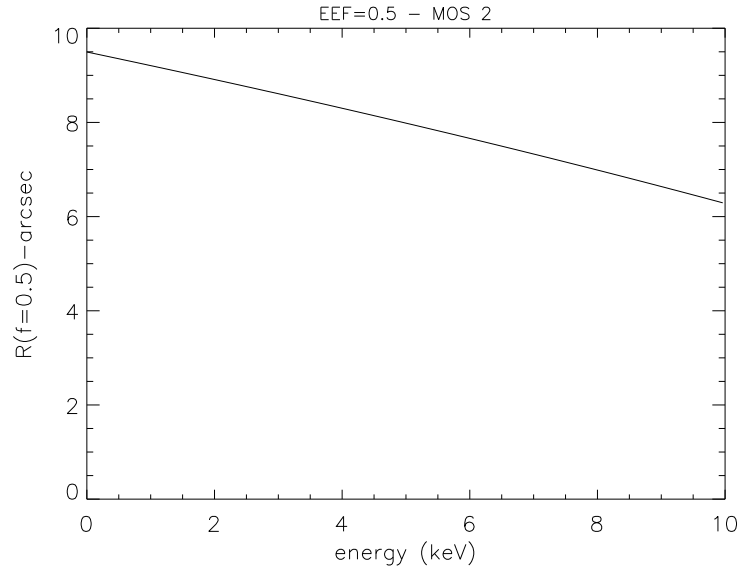
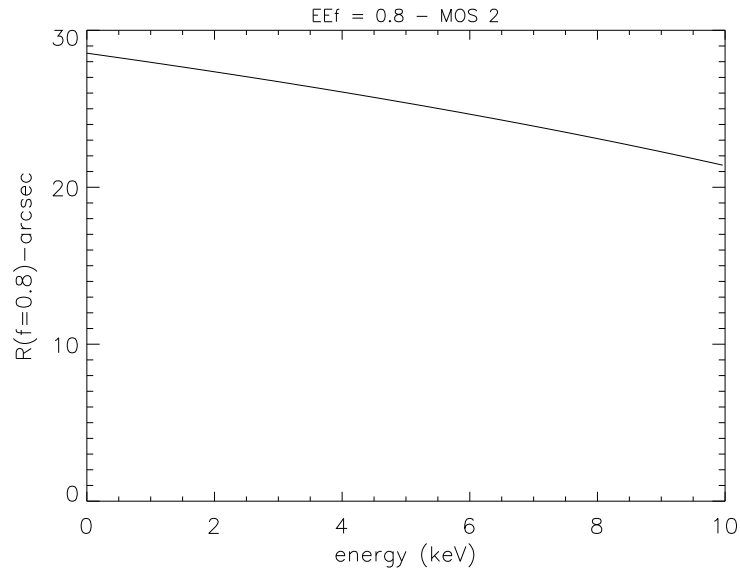Figure 25: Radius enclosing 50% of energy (arcsec units) for the on-axis position for MOS 2.

Figure 26: Radius enclosing 80% of energy (arcsec units) for the on-axis position for MOS 2.

Table 2: Radii enclosing 50% and 80% of the energy for MOS 1 and MOS 2 at the energies of 1.5, 8 , 9 keV, for the on-axis PSF.

MOS 1					
$R(50\%)$			$R(80\%)$		
1.5 keV	8 keV	9 keV	1.5 keV	8 keV	9 keV
8.6″	6.7″	6.4″	24.5″	21.5″	20.9″
MOS 2					
$R(50\%)$			$R(80\%)$		
1.5 keV	8 keV	9 keV	1.5 keV	8 keV	9 keV
9.1″	7.0″	6.6″	27.7″	23.1″	22.3″

$$EEF(R) = \frac{\displaystyle\int_{R_L}^{R} \frac{1}{\left[1+\left(\frac{r}{r_c}\right)^2\right]^\alpha} r\, dr}{\displaystyle\int_{0}^{R_N} \frac{1}{\left[1+\left(\frac{r}{r_c}\right)^2\right]^\alpha} r\, dr}. \tag{12}$$

By integrating this equation, we obtain:

$$EEF(R) = \frac{\dfrac{1}{\left[1+\left(\frac{R_L}{r_c}\right)^2\right]^{\alpha-1}} - \dfrac{1}{\left[1+\left(\frac{R}{r_c}\right)^2\right]^{\alpha-1}}}{1 - \dfrac{1}{\left[1+\left(\frac{R_N}{r_c}\right)^2\right]^{\alpha-1}}}. \tag{13}$$

From this equation, the radius R enclosing a fraction f of the energy can be derived:

$$R(f; r_c, \alpha) = r_c \left\{ \left[\frac{1}{\left[1+\left(\frac{R_L}{r_c}\right)^2\right]^{\alpha-1}} - f\left(1 - \frac{1}{\left[1+\left(\frac{R_N}{r_c}\right)^2\right]^{\alpha-1}}\right)\right]^{\frac{1}{1-\alpha}} - 1 \right\}^{\frac{1}{2}}, \tag{14}$$

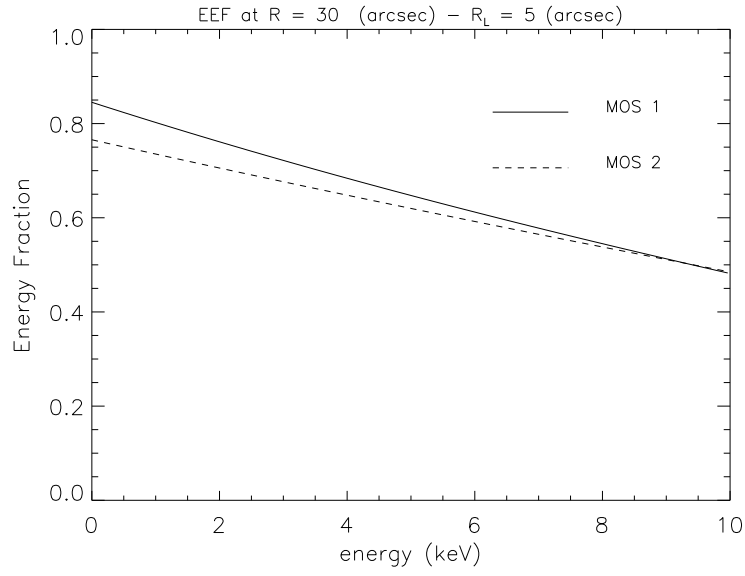which reduces to eqn. (11) for $R_L = 0$.

Figure 27: Energy fraction enclosed in the annulus within $[5'' - 30'']$ for MOS 1 (solid line) and MOS 2 (dashed line).
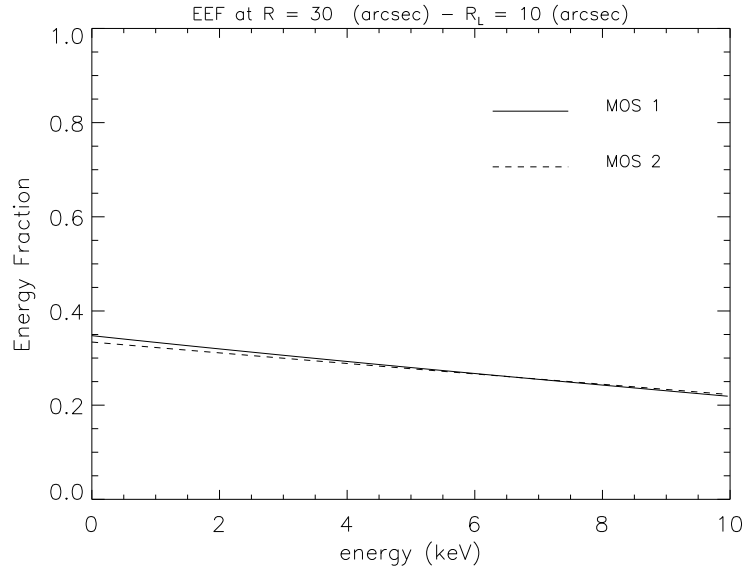

Figure 28: Energy fraction enclosed in the annulus within $[10'' - 30'']$ for MOS 1 (solid line) and MOS 2 (dashed line).

According to the different pile-up levels, R_L can be $5'', 10'', 20''$ or $30''$. In Figs. 27 and 28, I plotted the energy fraction enclosed within the annulus $[R_L, R]$ for $R = 30''$ and $R_L = 5', 10''$ (plots refer to the on-axis position). Other plots for different values are given in Appendix A.

These figures show that the EEF within $[R_L, R]$ decreases as energy increase. This is expected since, at higher energies the ability of the telescope in focusing photons increases. Correspondingly, a larger fraction of the energy is collected within R_L and the fraction in $[R_L, R]$ diminishes.

4.5.2 MOS 2 vs. MOS 1

Figs. 23-26 and Table 2 show that, at each energy, the energy fraction enclosed within a certain radius R is smaller for the MOS 2 (or equivalently, the radius enclosing a certain fraction of energy is smaller for the MOS 1). So, the MOS 1 behavior is slightly better than that of the MOS 2, contrary to expectations from ground calibration. Also preliminary results on in-orbit data by Aschenbach et al. (2000; *Proc. SPIE*, 4012, pg. 731) argued that MOS 2 had the best performance. However, their Table 2 shows that the difference between MOS 1 and MOS 2 from preliminary in-orbit data analysis, was reduced with respect to that found from ground calibration. Moreover, Aschenbach et al. (2000) data included only Small Window measures. Our data set is surely wider and Small Window measures suffer of a poor estimation of the background which can affect the best fit parameters.

The difference in EEF for the two cameras lies in their different slope behavior. Values reported in Table 1 show that MOS 2 has a smaller core but also a smaller α. The flatter trend on the wings for MOS 2 diminishes the encircled energy fraction at large radii.

The flatter wings for MOS 2 can be clearly observed in Figs. 29 and 30. In the top panels the profiles of the two sources HR1099 and LMC X-3 are plotted, for MOS 1 (black points) and MOS 2 (magenta points). In the bottom panels, the ratios of the profiles MOS1/MOS2 are plotted. In both cases, it can be seen clearly that on the wings the ratio is decreasing. Correspondingly the profiles are flatter for MOS 2 than for MOS 1.
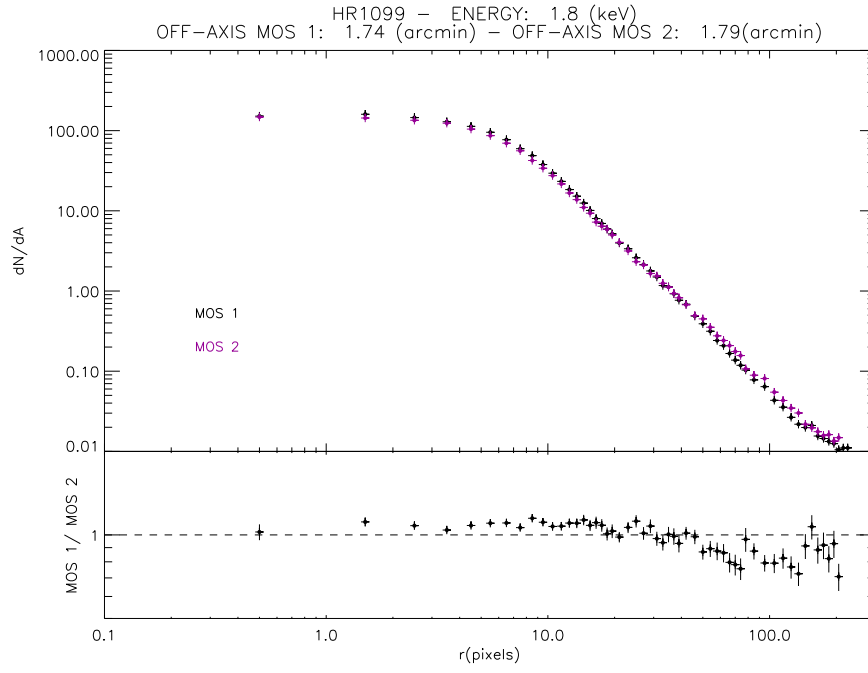
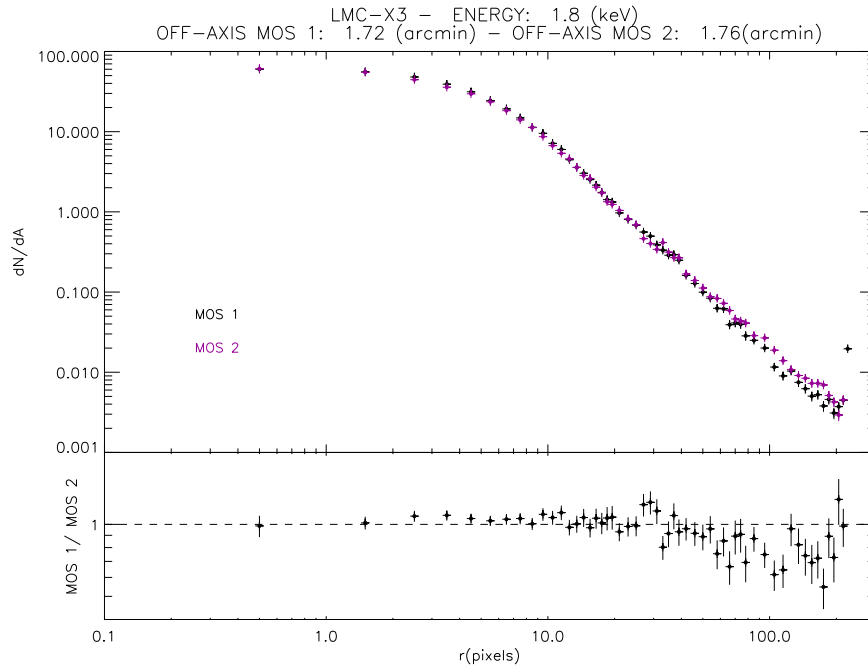Figure 29: Comparison between the profiles of HR1099 for MOS 1 and MOS 2.

Figure 30: Comparison between the profiles of LMC X-3 for MOS 1 and MOS 2.

41

A   Appendix: Plots.

In this Appendix, I collected some useful plots.
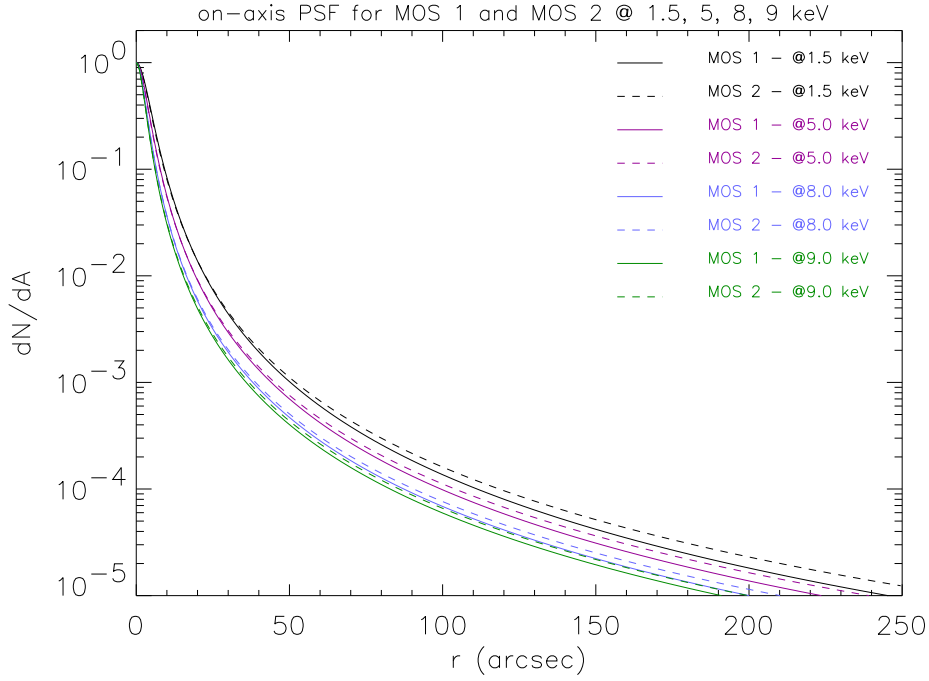
A.1   Plots for the PSF

Figure 31: On-axis PSF for the two MOS cameras at the energies: $1.5, 5, 8, 9$ keV. Solid lines refer to MOS 1; dashed lines to MOS 2.
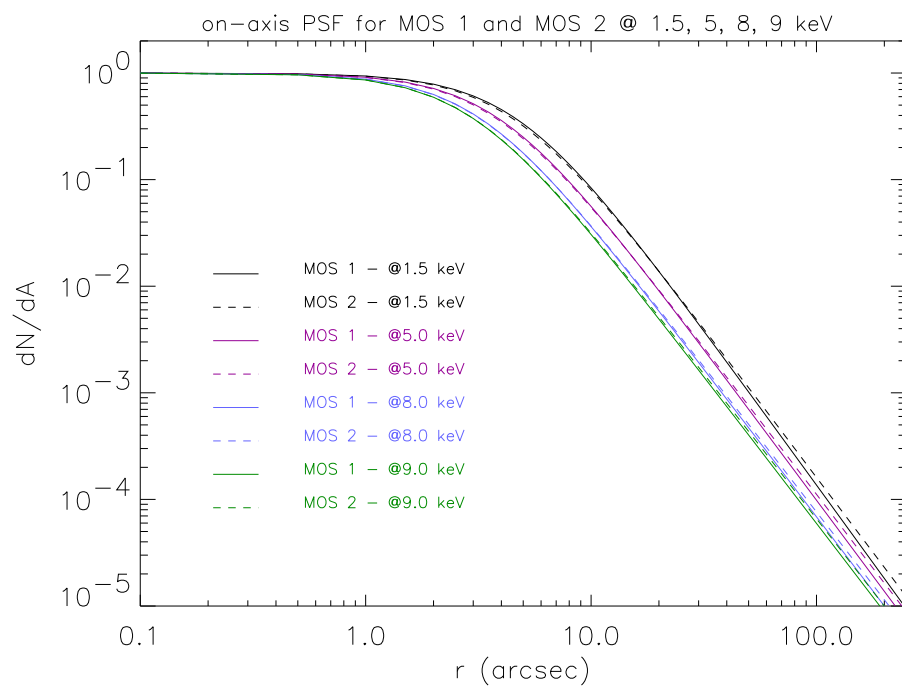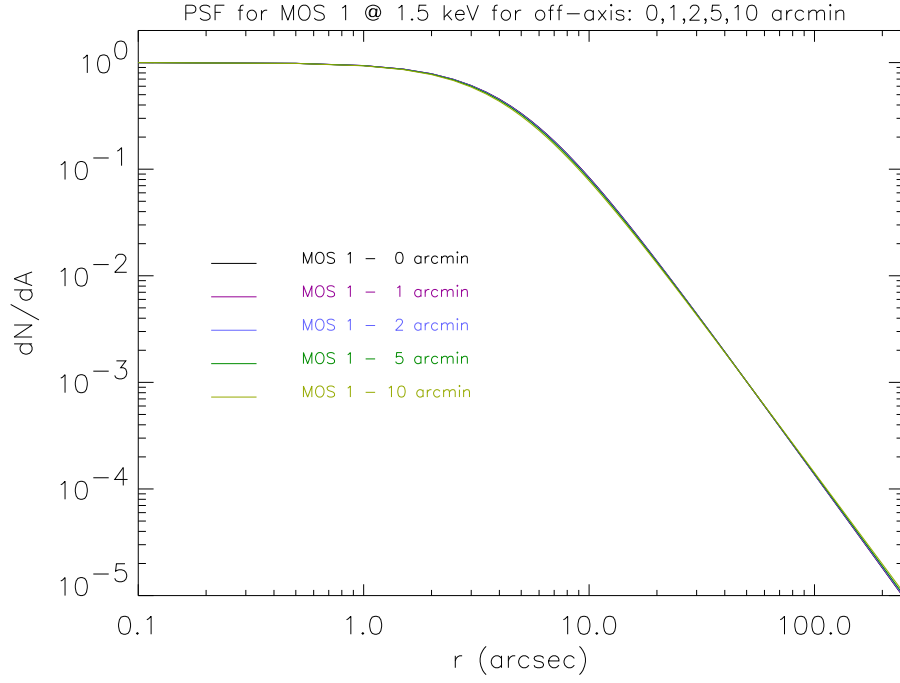
Figure 32: Same as Fig. 31, in logarithmic scale.

Figure 33: PSF for MOS 1 at the energy of 1.5 keV, at $0, 1, 2, 5, 10$ arcmin off-axis angles. Note that at low energies the PSF doesn't show significant variations with the off-axis angles. In fact, at these energies variations of the core radius and of the slope with the off-axis angles are really modest.

Figure 34: PSF for MOS 2 at the energy of 1.5 keV, at $0, 1, 2, 5, 10$ arcmin off-axis angles. As for the MOS 1, at low energies the PSF doesn't show significant variations with the off-axis angles. In fact, at these energies variations of the core radius and of the slope with the off-axis angles are really modest.
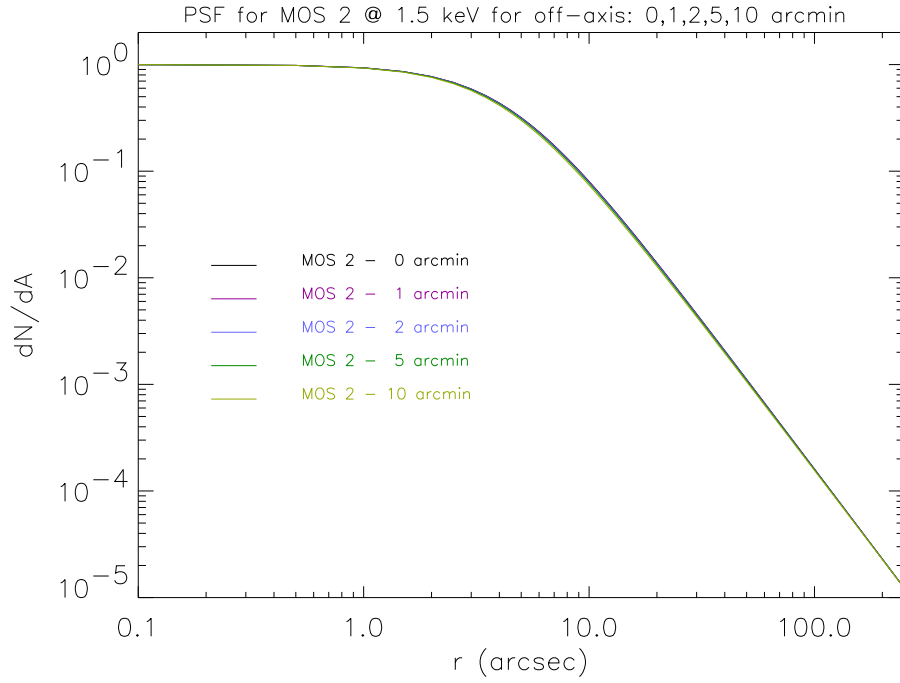
Figure 35: PSF for MOS 1 at the energy of 5 keV, at 0, 1, 2 arcmin off-axis angles. Also in this case the variations of the PSF seems negligible, but because of the range of application (see §4.4) only off-axis angles up to 2′ can be considered at these energies.
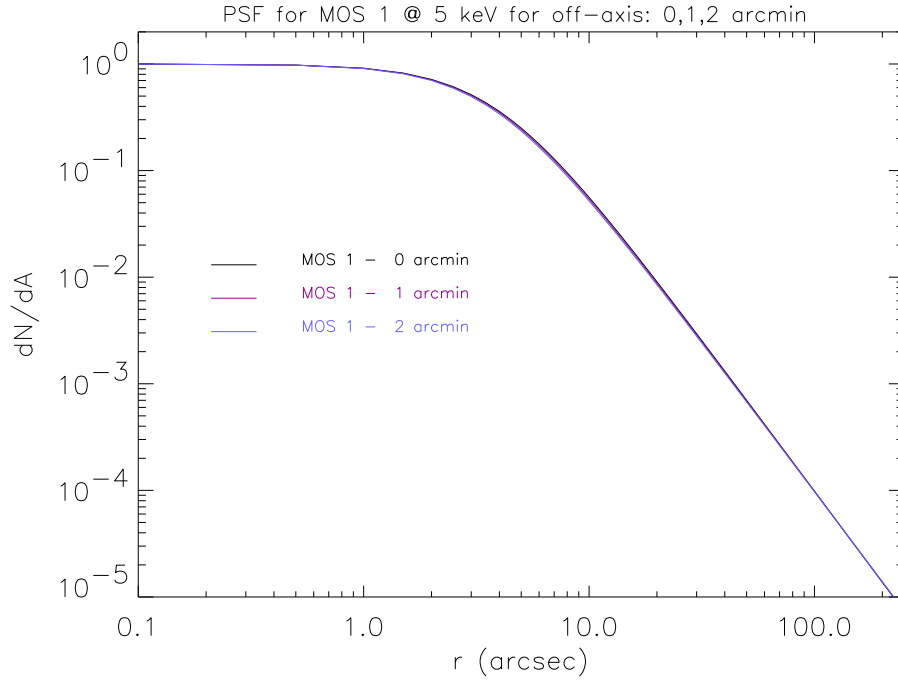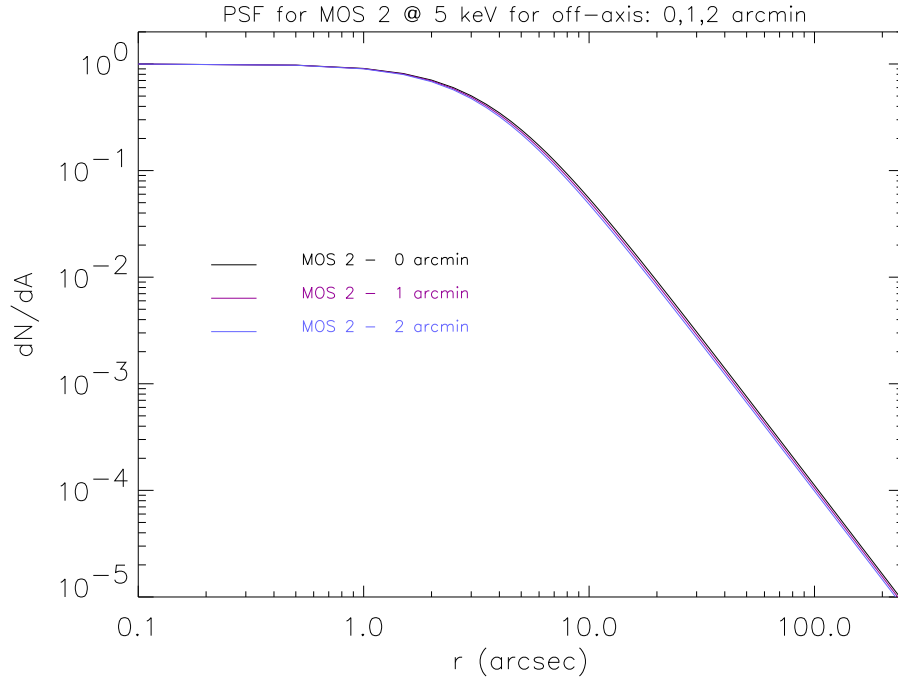
Figure 36: PSF for MOS 2 at the energy of 5 keV, at 0, 1, 2 arcmin off-axis angles. Also in this case the variations of the PSF seems negligible, but because of the range of application (see §4.4) only off-axis angles up to 2′ can be considered at these energies.

A.2 Plots for the EEF
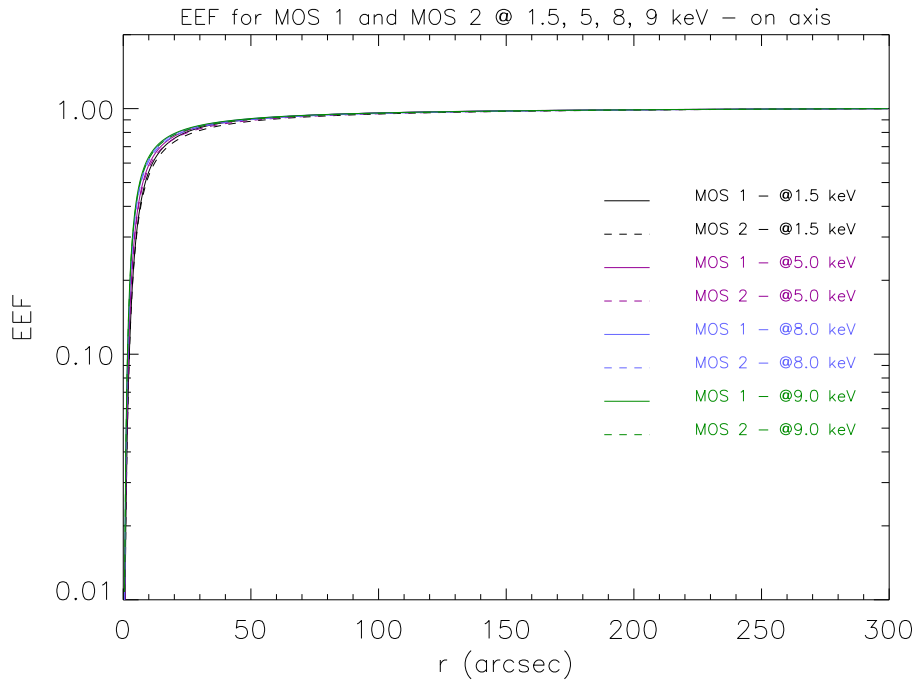
Figure 37: EEF for the two MOS cameras at the energies: $1.5, 5, 8, 9$ keV, for the on-axis position. Solid lines refer to MOS 1; dashed lines to MOS 2.
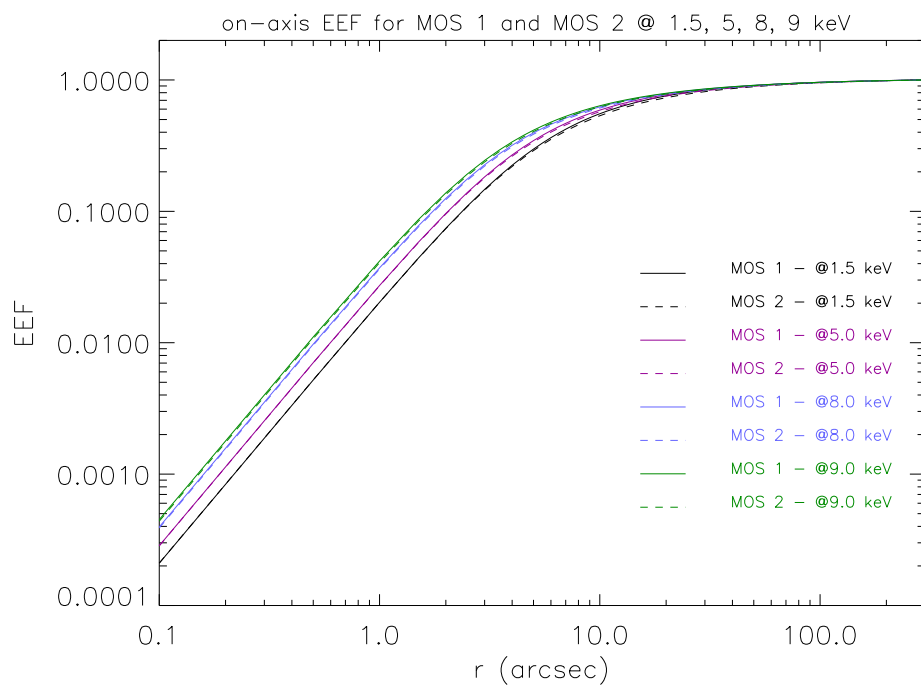
Figure 38: Same as Fig. 37, in logarithmic scale.
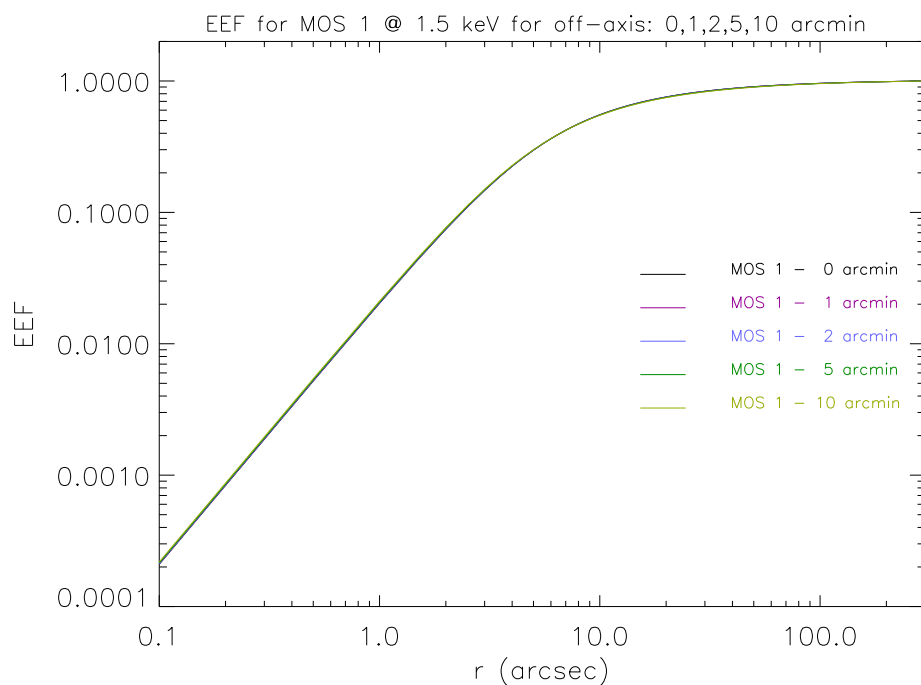
Figure 39: EEF for MOS 1 at the energy of 1.5 keV, at 0, 1, 2, 5, 10 arcmin off-axis angles.
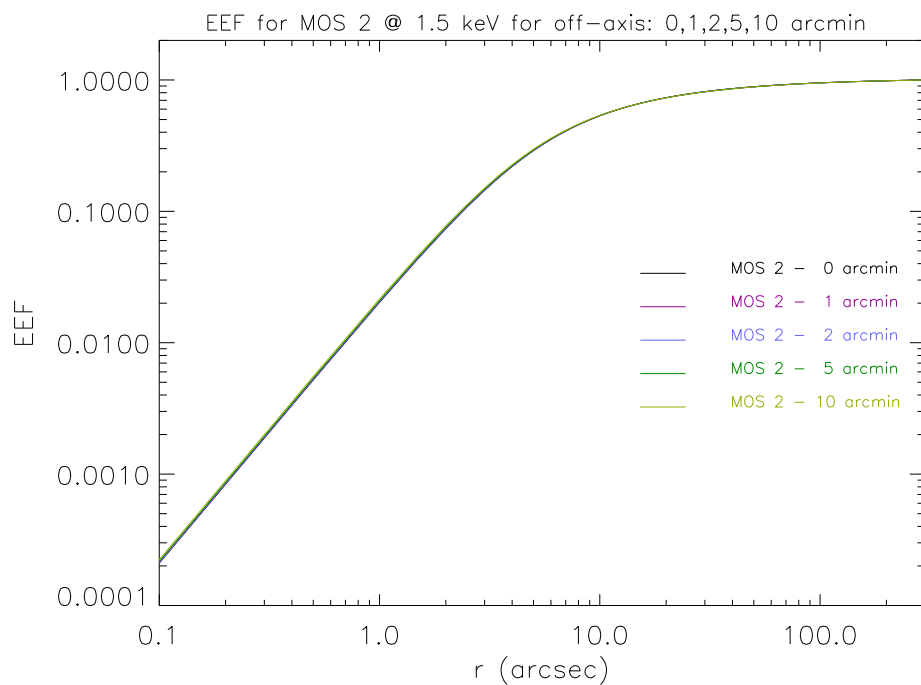
Figure 40: EEF for MOS 2 at the energy of 1.5 keV, at 0, 1, 2, 5, 10 arcmin off-axis angles.
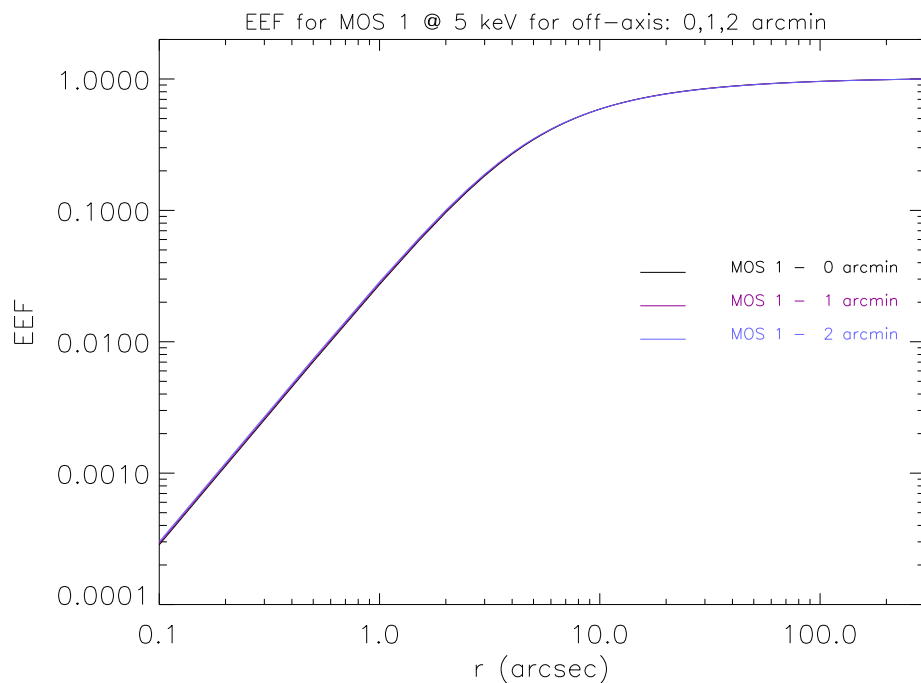
Figure 41: EEF for MOS 1 at the energy of 5 keV, at 0, 1, 2 arcmin off-axis angles.
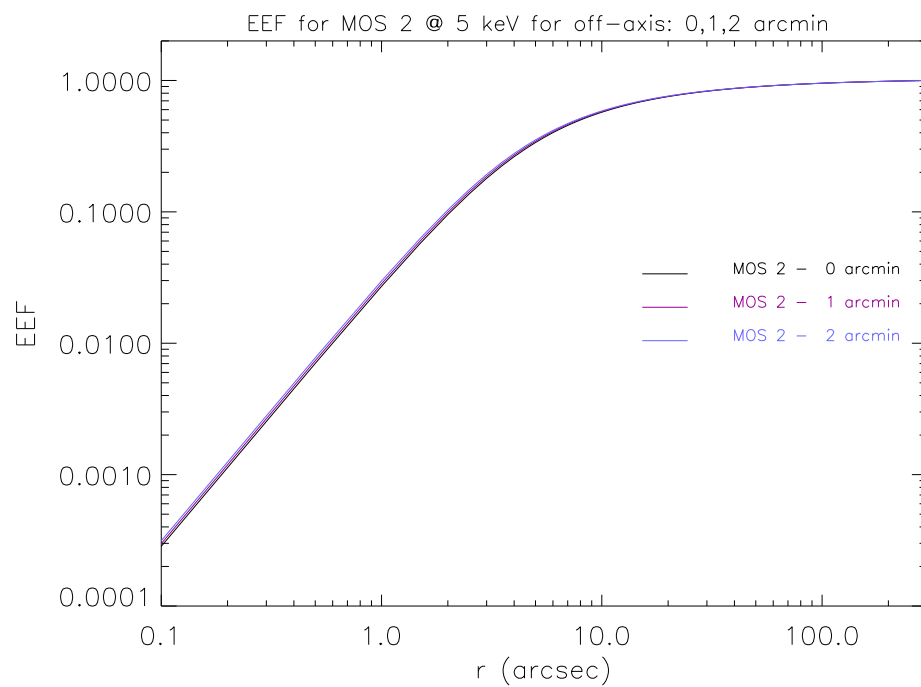
Figure 42: EEF for MOS 2 at the energy of 5 keV, at 0, 1, 2 arcmin off-axis angles.

A.3 Plots for the radius R enclosing a fraction f of the energy.

R50 for MOS 1–MOS 2 for off-axis: 0,1,2,5,10 arcmin

Legend:
- MOS 1 – 0 arcmin
- MOS 2 – 0 arcmin
- MOS 1 – 1 arcmin
- MOS 2 – 1 arcmin
- MOS 1 – 2 arcmin
- MOS 2 – 2 arcmin
- MOS 1 – 5 arcmin
- MOS 2 – 5 arcmin
- MOS 1 – 10 arcmin
- MOS 2 – 10 arcmin
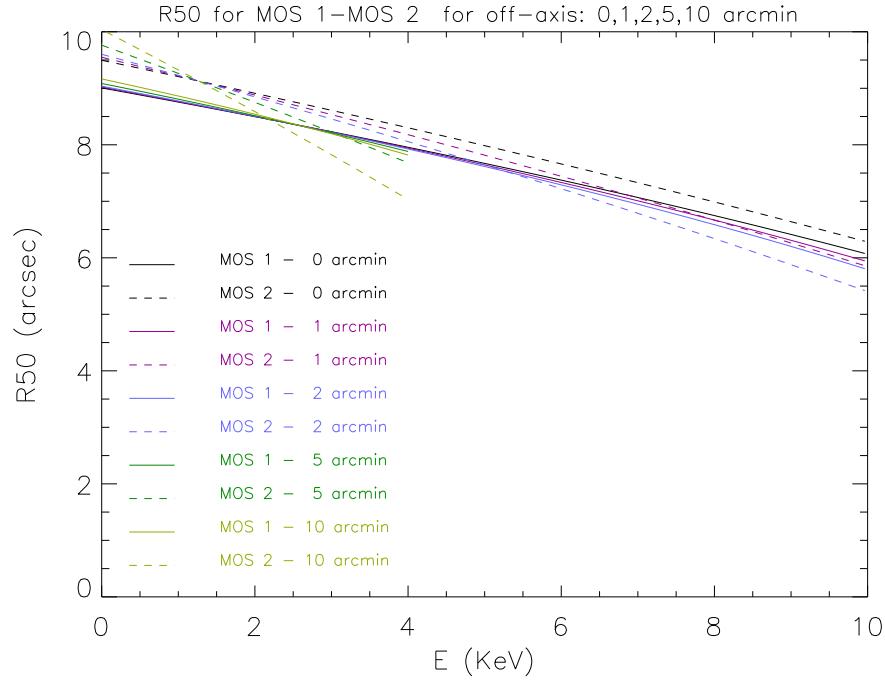
Figure 43: Radius enclosing 50% of the total energy for the two MOS cameras for $0, 1, 2, 5, 10$ off-axis angles. Solid lines refer to MOS 1; dashed lines to MOS 2. For off-axis angles the lines are truncated according to the range of application defined in §4.4.
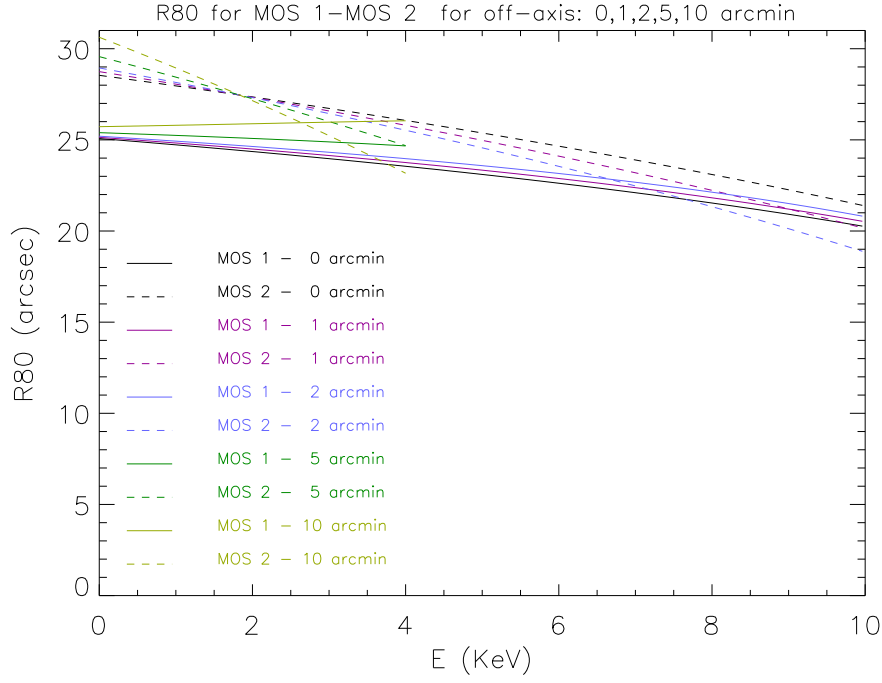
Figure 44: Radius enclosing 80% of the total energy for the two MOS cameras for
0, 1, 2, 5, 10 off-axis angles. Solid lines refer to MOS 1; dashed lines to MOS 2. For
off-axis angles the lines are truncated according to the range of application defined in
§4.4.
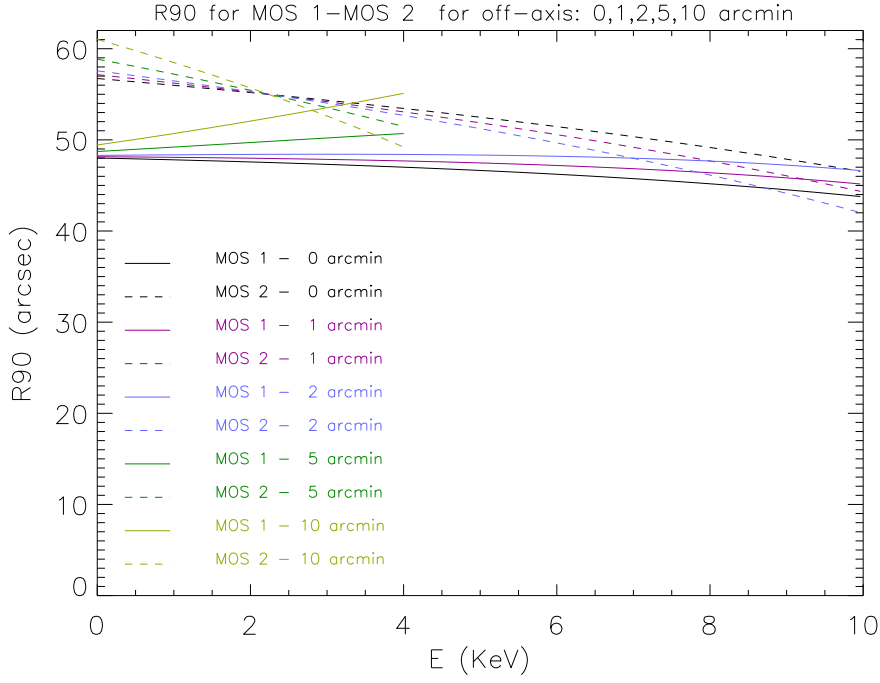
Figure 45: Radius enclosing 90% of the total energy for the two MOS cameras for 0, 1, 2, 5, 10 off-axis angles. Solid lines refer to MOS 1; dashed lines to MOS 2. For off-axis angles the lines are truncated according to the range of application defined in §4.4.

A.4 Plots for the EEF for piled-up sources
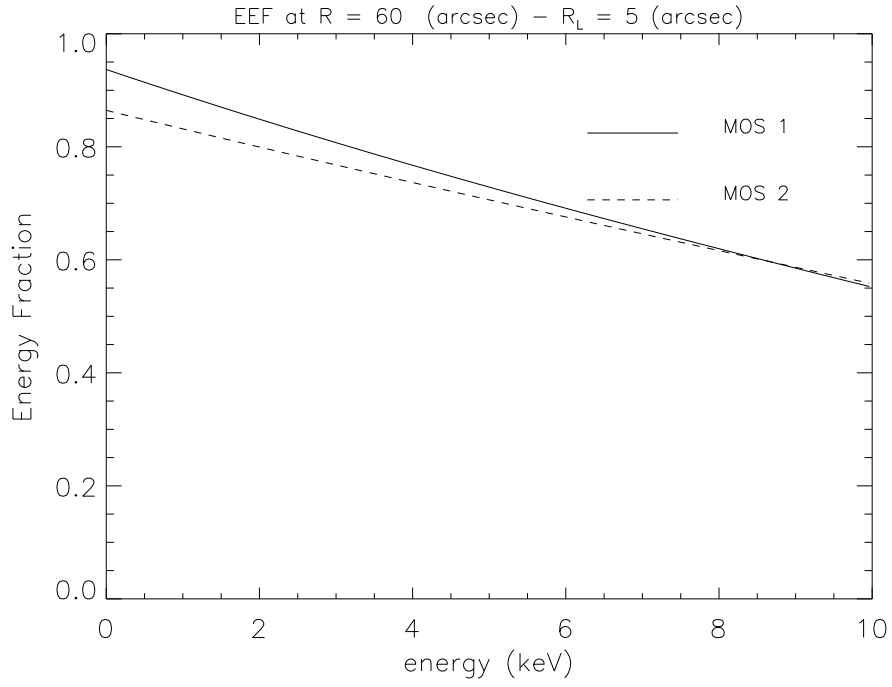
Figure 46: Energy fraction enclosed in the annulus within $[5'' - 60'']$ for MOS 1 (solid line) and MOS 2 (dashed line).
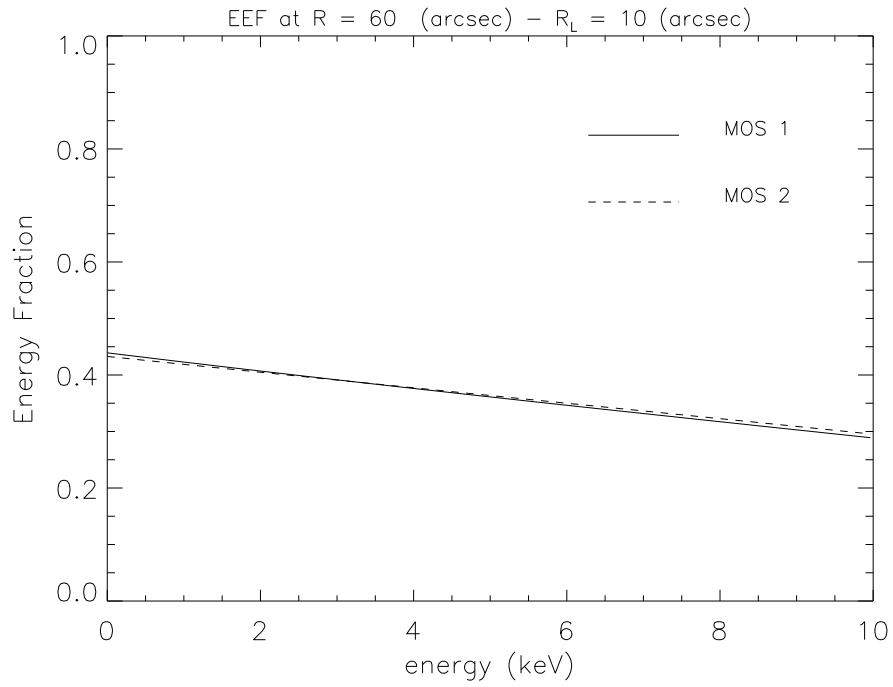
Figure 47: Energy fraction enclosed in the annulus within $[10'' - 60'']$ for MOS 1 (solid line) and MOS 2 (dashed line).
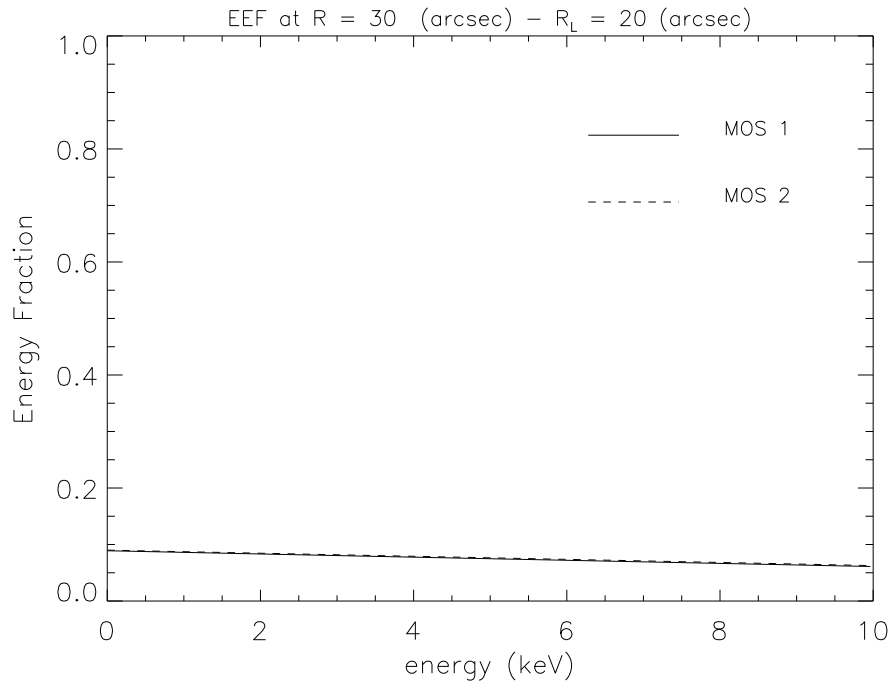
Figure 48: Energy fraction enclosed in the annulus within $[20'' - 30'']$ for MOS 1 (solid line) and MOS 2 (dashed line).
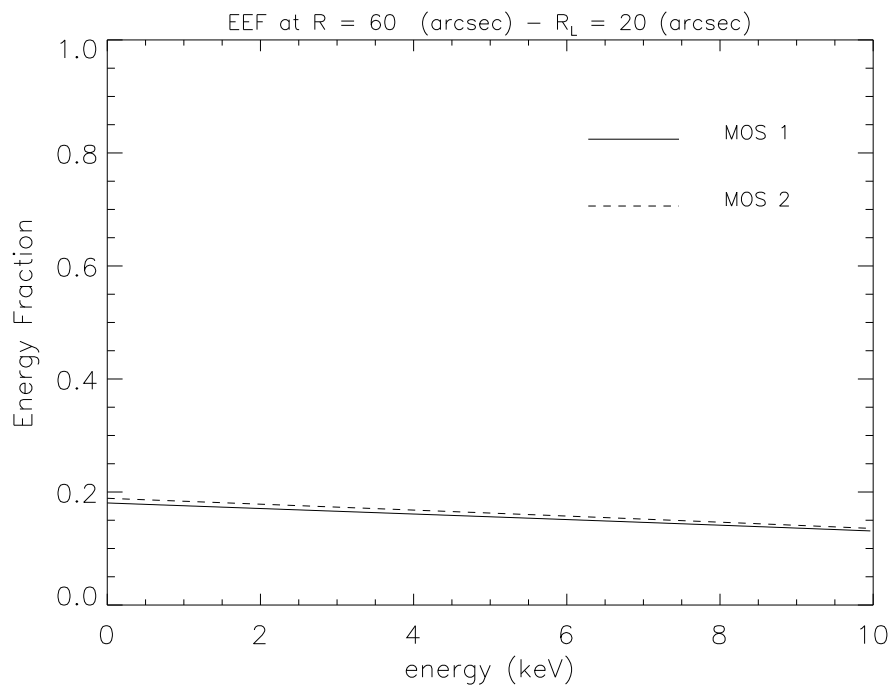
Figure 49: Energy fraction enclosed in the annulus within $[20'' - 60'']$ for MOS 1 (solid line) and MOS 2 (dashed line).
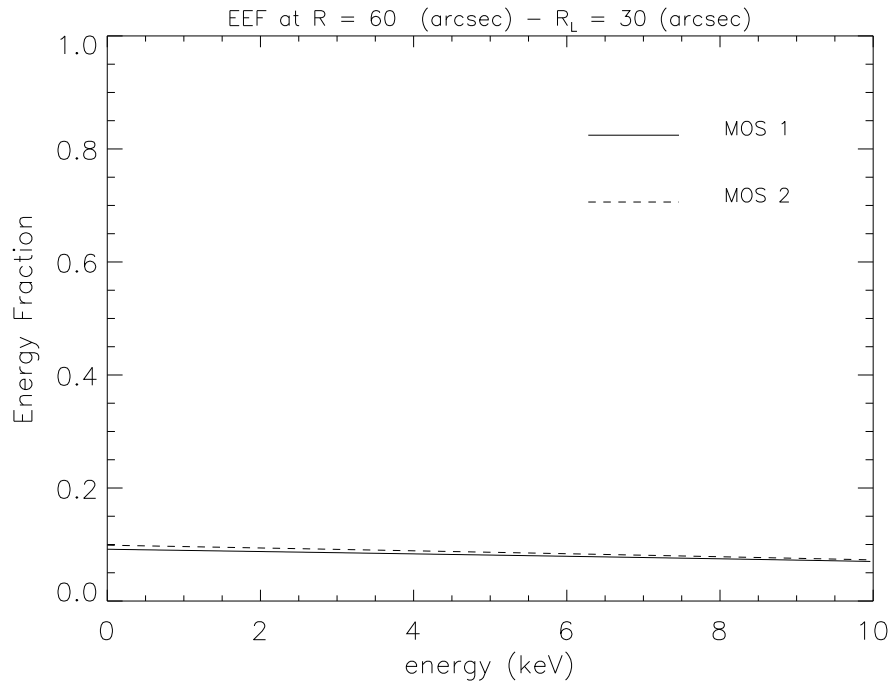
Figure 50: Energy fraction enclosed in the annulus within $[30'' - 60'']$ for MOS 1 (solid line) and MOS 2 (dashed line).
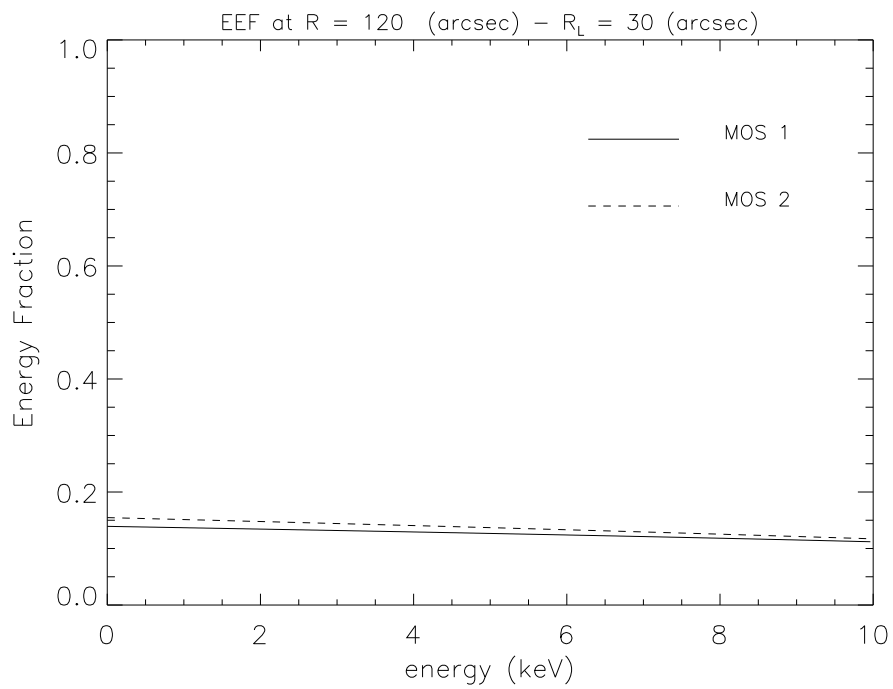
Figure 51: Energy fraction enclosed in the annulus within $[30'' - 120'']$ for MOS 1 (solid line) and MOS 2 (dashed line).

Table 3: List of the observations (see Sec. 2 for details).

| source	RUNID	MOS	off-axis (arcmin)	OP. mode
Capella	00430119700301EMOS1U009	1	1.70	FF
Capella	00430119700401EMOS1S005	1	1.70	DN
Capella	00430119700401EMOS1S007	1	1.70	LW
Capella	00430119700401EMOS1S009	1	1.70	LW
Capella	00430119700401EMOS1S013	1	1.69	FF
Capella	00460120900201EMOS1S005	1	1.16	DN
Capella	00460120900201EMOS1S008	1	1.16	LW
Capella	00460120900201EMOS1U029	1	1.16	DN
Capella	00460120900201EMOS1S010	1	1.20	FF
Capella	00540121920101EMOS1U009	1	0.12	FF
Capella	00430119700201EMOS2U009	2	1.49	FF
Capella	00430119700301EMOS2U004	2	1.49	FF
Capella	00430119700401EMOS2S006	2	1.49	DN
Capella	00430119700401EMOS2S008	2	1.49	LW
Capella	00430119700401EMOS2S010	2	1.49	LW
Capella	00430119700401EMOS2S014	2	1.35	FF
Capella	00460120900201EMOS2S007	2	1.24	DN
Capella	00460120900201EMOS2S009	2	1.24	LW
Capella	00460120900201EMOS2U027	2	1.24	DN
Capella	00460120900201EMOS2S011	2	1.49	FF
EXO0748-67	00440119710201EMOS1U013	1	1.14	FF
EXO0748-67	00440119710201EMOS2U013	2	0.94	FF
EXO0748-67	00550122310301EMOS2U004	2	0.76	FF

Table 3 (continue). List of the observations

source	RUNID	MOS	off-axis (arcmin)	OP. mode
EXO0748-67	00370118300401EMOS1S003	1	0.71	FF
EXO0748-67	00370118300501EMOS1S003	1	0.71	FF
EXO0748-67	00370118300601EMOS1S003	1	0.71	FF
EXO0748-67	00370118300701EMOS1S003	1	0.71	FF
EXO0748-67	00380117900801EMOS1S006	1	0.71	FF
EXO0748-67	00380117900801EMOS1U002	1	0.71	FF
EXO0748-67	00380117900901EMOS1S006	1	0.71	FF
EXO0748-67	00400118700601EMOS1S003	1	0.71	FF
EXO0748-67	00370118300401EMOS2S004	2	0.77	FF
EXO0748-67	00370118300501EMOS2S004	2	0.77	FF
EXO0748-67	00370118300601EMOS2S004	2	0.77	FF
EXO0748-67	00370118300701EMOS2S004	2	0.77	FF
EXO0748-67	00380117900801EMOS2S007	2	0.77	FF
EXO0748-67	00380117900801EMOS2U002	2	0.77	FF
EXO0748-67	00380117900901EMOS2S007	2	0.77	FF
EXO0748-67	00400118700601EMOS2S004	2	0.77	FF
HR1099	00279002700001EMOS1U009	1	1.72	FF
HR1099	00280116340601EMOS1S002	1	1.72	FF
HR1099	00300116710901EMOS1S008	1	1.72	LW
HR1099	00310116890901EMOS1S006	1	0.17	FF
HR1099	00310116890901EMOS1S007	1	0.17	SW
HR1099	00310116890901EMOS1S011	1	0.17	SW
HR1099	00310116891001EMOS1S005	1	0.17	LW
HR1099	00279002700001EMOS2U009	2	1.78	FF
HR1099	00280116340601EMOS2S004	2	1.78	FF
HR1099	00300116710901EMOS2S012	2	1.78	FF

Table 3 (continue). List of the observations

source	RUNID	MOS	off-axis (arcmin)	OP. mode
HR1099	00310116890901EMOS2S009	2	0.11	FF
HR1099	00310116890901EMOS2S010	2	0.11	SW
HR1099	00310116890901EMOS2S012	2	0.11	SW
HR1099	00310116891001EMOS2S007	2	0.11	LW
LMC X-3	00280113620201EMOS1S004	1	1.65	FF
LMC X-3	00280113620301EMOS1S007	1	1.65	DN
LMC X-3	00280113620301EMOS1U003	1	1.65	LW
LMC X-3	00280113620301EMOS1S008	1	1.81	FF
LMC X-3	00300116900501EMOS1S007	1	0.27	LW
LMC X-3	00410118900401EMOS1S003	1	0.25	SW
LMC X-3	00410118900401EMOS1S005	1	0.25	LW
LMC X-3	00410118900401EMOS1S007	1	0.25	SW
LMC X-3	00450120300201EMOS1S003	1	0.25	FF
LMC X-3	00450120300301EMOS1S007	1	0.25	LW
LMC X-3	00410118900401EMOS1S010	1	0.35	FF
LMC X-3	00280113620201EMOS2S009	2	1.78	FF
LMC X-3	00280113620301EMOS2S012	2	1.78	DN
LMC X-3	00280113620301EMOS2U003	2	1.78	LW
LMC X-3	00280113620301EMOS2S013	2	1.86	FF
LMC X-3	00300116900501EMOS2S009	2	0.13	LW
LMC X-3	00410118900401EMOS2S004	2	0.08	SW
LMC X-3	00410118900401EMOS2S006	2	0.08	LW
LMC X-3	00410118900401EMOS2S008	2	0.08	SW
LMC X-3	00450120300201EMOS2S004	2	0.08	FF
LMC X-3	00450120300301EMOS2S008	2	0.08	LW
LMC X-3	00410118900401EMOS2S011	2	0.13	FF

Table 3 (continue). List of the observations

source	RUNID	MOS	off-axis (arcmin)	OP. mode
PKS0312	00570122520201EMOS1S001	1	0.08	FF
PKS0312	00570122520201EMOS2S002	2	0.31	FF
PKS0558-504	00300116700301EMOS1S005	1	1.70	FF
PKS0558-504	00300116700301EMOS1S006	1	1.70	DN
PKS0558-504	00320117500201EMOS1S017	1	0.24	DN
PKS0558-504	00320117500201EMOS1S018	1	0.24	LW
PKS0558-504	00330117710601EMOS1S039	1	0.24	FF
PKS0558-504	00330117710601EMOS1S040	1	0.24	LW
PKS0558-504	00330117710601EMOS1S041	1	0.24	SW
PKS0558-504	00330117710601EMOS1S042	1	0.24	LW
PKS0558-504	00330117710601EMOS1S043	1	0.24	SW
PKS0558-504	00420119100201EMOS1S003	1	0.24	FF
PKS0558-504	00420119100201EMOS1U002	1	0.24	FF
PKS0558-504	00420119100301EMOS1S019	1	0.24	LW
PKS0558-504	00420119100301EMOS1U008	1	0.24	FF
PKS0558-504	00420119100301EMOS1U009	1	0.24	SW
PKS0558-504	00450120300801EMOS1S005	1	0.24	FF
PKS0558-504	00450120300801EMOS1S009	1	0.24	FF
PKS0558-504	00300116700301EMOS2S008	2	1.74	FF
PKS0558-504	00300116700301EMOS2S009	2	1.74	DN
PKS0558-504	00330117710701EMOS2S043	2	0.17	FF
PSR0540	00320117510201EMOS1S005	1	0.31	FF
PSR0540	00320117510201EMOS1S006	1	0.38	SW
PSR0540	00320117510201EMOS1S017	1	0.38	SW
PSR0540	00350117730501EMOS1S014	1	0.27	FF
PSR0540	00350117730501EMOS1S016	1	0.27	SW

Table 3 (continue). List of the observations

source	RUNID	MOS	off-axis (arcmin)	OP. mode
PSR0540	00410118900701EMOS1S003	1	0.34	SW
PSR0540	00320117510201EMOS2S007	2	0.19	FF
PSR0540	00320117510201EMOS2S009	2	0.36	SW
PSR0540	00320117510201EMOS2S021	2	0.36	SW
PSR0540	00350117730501EMOS2S015	2	0.09	FF
PSR0540	00350117730501EMOS2S017	2	0.09	SW
PSR0540	00410118900701EMOS2S004	2	0.14	SW
PKS0558-504	00320117500201EMOS2S021	2	0.02	DN
PKS0558-504	00320117500201EMOS2S022	2	0.02	SW
PKS0558-504	00330117710701EMOS2S038	2	0.02	FF
PKS0558-504	00330117710701EMOS2S039	2	0.02	LW
PKS0558-504	00330117710701EMOS2S040	2	0.02	SW
PKS0558-504	00330117710701EMOS2S041	2	0.02	LW
PKS0558-504	00330117710701EMOS2S042	2	0.02	SW
PKS0558-504	00420119100201EMOS2S018	2	0.02	FF
PKS0558-504	00420119100201EMOS2U002	2	0.02	FF
PKS0558-504	00420119100201EMOS2U003	2	0.02	FF
PKS0558-504	00420119100301EMOS2S020	2	0.02	SW
PKS0558-504	00420119100301EMOS2U009	2	0.02	FF
PKS0558-504	00420119100301EMOS2U010	2	0.02	FF
PKS0558-504	00420119100301EMOS2U018	2	0.02	FF
PKS0558-504	00420119100301EMOS2U019	2	0.02	SW
PKS0558-504	00450120300801EMOS2S006	2	0.02	FF
PKS0558-504	00450120300801EMOS2S010	2	0.02	FF
LMC1	00220115740201EMOS1U009	1	11.89	FF
LMC1	00229999990019EMOS1U002	1	11.89	FF

Table 3 (continue). List of the observations

source	RUNID	MOS	off-axis (arcmin)	OP. mode
LMC1	00220115740201EMOS2S007	2	11.90	FF
LMC1	00220115740201EMOS2U002	2	11.90	FF
LMC1	00229999990019EMOS2U003	2	11.90	FF
LMC2	00220115740201EMOS2S007	2	5.56	FF
LMC2	00220115740201EMOS2U002	2	5.56	FF
LMC2	00229999990019EMOS2U003	2	5.56	FF
HCG016	0023011581030103EMOS1S009	1	11.52	FF
HCG016	00239999990021EMOS1U002	1	11.52	FF
HCG016	00230115810301EMOS2S007	2	11.57	FF
HCG016	00230115810301EMOS2U002	2	11.57	FF
PSR0540	00410118901101EMOS1S003	1	9.83	TI
PSR0540	00410118901201EMOS1U002	1	9.83	TI
PSR0540	00410118901101EMOS2S004	2	9.85	TI
PSR0540	00410118901201EMOS2U002	2	9.85	TI
Capella2	00530121500301EMOS1S003	1	9.48	FF
Capella2	00530121500301EMOS2S004	2	9.57	FF
GX13+1b	00560122340501EMOS2S004	2	3.15	FF
GX13+1b	00580122340701EMOS1S003	1	2.74	FF
GX13+1b	00580122340701EMOS2S004	2	2.71	FF
3C273	00940126700201EMOS1S001	1	1.55	FF
3C273	00940126700201EMOS2S002	2	1.54	FF
3C273	00950126700701EMOS1S001	1	0.15	SW
3C273	00950126700701EMOS2S002	2	0.15	SW
OMC2/3	02370093000101EMOS1S001	1	[2.03 - 10.42]	FF
OMC2/3	02370093000101EMOS2S003	2	[0.34 - 10.44]	FF